

nature medicine

















Wireless biosensors in the neonatal ICU

Blood-based biomarkers for Alzheimer's

Salt substitution effect on blood pressure and hypertension



Skin-interfaced biosensors for advanced wireless physiological monitoring in neonatal and pediatric intensive-care units

Ha Uk Chung ^{1,2,3,28}, Alina Y. Rwei^{1,3,28}, Aurélie Hourlier-Fargette ^{1,3,28}, Shuai Xu^{1,3,4,28}, KunHyuck Lee ^{1,3,5}, Emma C. Dunne⁶, Zhaoqian Xie ⁷, Claire Liu ^{1,3,8}, Andrea Carlini^{1,3,5}, Dong Hyun Kim^{3,9}, Dennis Ryu^{3,10}, Elena Kulikova¹⁰, Jingyue Cao¹⁰, Ian C. Odland³, Kelsey B. Fields^{3,5}, Brad Hopkins⁶, Anthony Banks^{1,3}, Christopher Ogle³, Dominic Grande³, Jun Bin Park³, Jongwon Kim ^{11,12}, Masahiro Irie^{1,2,3}, Hokyung Jang^{3,13}, JooHee Lee¹⁰, Yerim Park¹⁴, Jungwoo Kim¹⁴, Han Heul Jo¹⁴, Hyoungjo Hahm⁹, Raudel Avila^{3,5,15,16}, Yeshou Xu^{3,5,15,16,17}, Myeong Namkoong^{1,8}, Jean Won Kwak ^{1,3,15}, Emily Suen¹⁸, Max A. Paulus¹⁹, Robin J. Kim³, Blake V. Parsons³, Kelia A. Human ⁸, Seung Sik Kim⁹, Manish Patel ^{1,3,5,10,20}, William Reuther ²¹, Hyun Soo Kim^{9,13}, Sung Hoon Lee⁹, John D. Leedle¹⁰, Yeojeong Yun¹³, Sarah Rigali¹⁰, Taeyoung Son¹³, Inhwa Jung¹², Hany Arafa^{1,3,8}, Vinaya R. Soundararajan⁴, Ayelet Ollech⁴, Avani Shukla²², Allison Bradley⁶, Molly Schau²³, Casey M. Rand^{6,24}, Lauren E. Marsillio^{22,25}, Zena L. Harris^{22,25}, Yonggang Huang ^{3,5,15,16}, Aaron Hamvas^{22,23,24}, Amy S. Paller^{3,5,22}, Debra E. Weese-Mayer ^{6,22,24} ✉, Jong Yoon Lee ^{1,3,9,10} ✉ and John A. Rogers ^{1,3,5,8,13,15,26,27} ✉

Standard clinical care in neonatal and pediatric intensive-care units (NICUs and PICUs, respectively) involves continuous monitoring of vital signs with hard-wired devices that adhere to the skin and, in certain instances, can involve catheter-based pressure sensors inserted into the arteries. These systems entail risks of causing iatrogenic skin injuries, complicating clinical care and impeding skin-to-skin contact between parent and child. Here we present a wireless, non-invasive technology that not only offers measurement equivalency to existing clinical standards for heart rate, respiration rate, temperature and blood oxygenation, but also provides a range of important additional features, as supported by data from pilot clinical studies in both the NICU and PICU. These new modalities include tracking movements and body orientation, quantifying the physiological benefits of skin-to-skin care, capturing acoustic signatures of cardiac activity, recording vocal biomarkers associated with tonality and temporal characteristics of crying and monitoring a reliable surrogate for systolic blood pressure. These platforms have the potential to substantially enhance the quality of neonatal and pediatric critical care.

In the United States, over 480,000 critically ill children receive care in ICUs each year, including premature neonates weighing as little as 500 g¹⁻³. Continuous monitoring of vital signs is essential, yet existing technologies require the use of multiple electrodes and sensor interfaces attached to the skin with adhesives connected by wires to electronic processing systems that are often tethered to the wall. This system of hardware often frustrates both routine and specialized procedures in clinical care, ranging from therapeutic skin-to-skin contact with parents (that is, kangaroo care (KC)) to feeding, diaper changes and bathing³. Furthermore, continuous monitoring of certain vital signs, such as blood pressure, demands additional wired tools, such as peripheral and umbilical arterial catheters⁴, which can induce other complications, including thrombus formation and blood-vessel occlusion, infection (for example sepsis), rupture, pseudoaneurysm, bleeding and death⁵⁻⁷. A wireless system capable of non-invasive, continuous, accurate vital-signs

monitoring has the potential to greatly enhance the safety and effectiveness of neonatal and pediatric critical care⁸.

A recent report by our group⁹ describes a soft, skin-like electronic system designed to address these unmet clinical needs. Evaluation studies in the NICU confirm capabilities for clinically accurate measurements of heart rate (HR), blood oxygenation (SpO₂), temperature, respiration rate (RR) and pulse-wave velocity. This system, however, is limited by (1) the modest maximum operating distances (~30 cm) supported by wireless power transfer and data communication, (2) the mechanically fragile nature of the ultrathin, compliant mechanics designs, (3) the sufficient, but limited, range of measurement capabilities and (4) the demand for advanced device configurations, capable of fabrication in only specialized facilities with customized tools. The results reported here adapt and extend similar principles in soft electronics design, but in mechanically robust, manufacturable systems that circumvent these

A full list of affiliations appears at the end of the paper.

shortcomings and provide additional capabilities. These systems include options in operation and power supply to address a broad spectrum of clinical-use cases and provider preferences, ranging from modular primary batteries to integrated secondary batteries to wireless power-harvesting schemes. These platforms additionally support important and new monitoring modalities beyond both the standard of care and the capabilities of our previously reported systems. These options include the ability to: (1) monitor movements and changes in body orientation, (2) track and assess the therapeutic effects of KC and other forms of hands-on care, (3) capture acoustic signatures associated with cardiac activity by sensing mechanical vibrations on the skin of the chest wall, (4) record vocal biomarkers associated with tonality and temporal characteristics of crying and (5) quantify pulse-wave dynamics through multiple measurements, as a surrogate for systolic blood pressure.

The ability of this system to provide additional quantitative information on hemodynamic and cardiovascular health states beyond the core vital signs of heart rate, respiratory rate and blood oximetry holds direct relevance to the management of patients in the NICU or PICU¹⁰. Visualization of heart vibrations, referred to as a seismocardiogram (SCG), is rarely performed in general clinical practice, especially in the NICU/PICU, yet it provides essential information on the mechanical outcomes of myocardial activity, valve motions and other features that are absent from ECG data¹¹. The capabilities of the system also address aspects of neurological, and cardiopulmonary disorders that are common in premature neonates and can lead to abnormalities in vocalization, range of motion and posture control¹². Quantitative, continuous tracking of such behavior offers the potential for early detection of complications associated with birth trauma, brain injury, pain or stress¹³. Measurements of movement and physical activity specifically can provide insights into sensorimotor development¹². These same data can also inform effective methods for neonatal care such as KC, a therapeutic skin-to-skin 'treatment' in which a pediatric patient is held against a parent's chest in a manner that lowers mortality, stabilizes heart rate, temperature and respiration rate, and decreases the risk of infection^{14,15}.

The following describes the technology platforms, measurement capabilities, clinical effectiveness and safety through pilot studies on 50 patients across a wide range of ages in both the NICU and the PICU. We present quantitative validation of the full range of capabilities, with comparisons to measurements recorded using Food and Drug Administration (FDA)-approved monitoring systems, for continuous monitoring periods of up to 24 h.

Results

Device and system design. Figure 1a presents an exploded-view illustration of one of the two mechanically soft, wireless devices that form the complete system. This example uses a modular battery unit for power supply in a design that allows for gentle placement on the curved skin of the chest (chest unit) via a thin, conductive hydrogel coupling layer to record electrocardiograms (ECGs), acoustic signals of vocalization and cardiac/respiratory activity, body orientation and movements and skin temperature, all enabled by a Bluetooth Low Energy (BLE) system-on-a-chip (SoC) and associated collection of sensors. The overall layout includes a thin, flexible printed circuit board (FPCB) and mounted components, configured in an open design with serpentine interconnect traces. The construction involves folding of distinct, but connected, platforms as a key step in assembly and packaging to reduce surface area—critical for placement on premature neonates (Fig. 1a and Extended Data Fig. 1a). An optimal distribution of the components reduces the lateral dimensions of the device by ~250%, guided by three-dimensional finite element analysis (FEA) of the system-level mechanics. A pre-compression process in the assembly forms buckled layouts in a serpentine configuration to enhance flexibility and stretchability. An elastomeric enclosure with an inner silicone-gel liner (~300 μm

thick, ~4 kPa) further improves the soft mechanical properties, ensuring compatibility with the fragile skin and the highly curved anatomical features of neonates born at the earliest gestational ages (GAs). A pair of thin, conductive elements, formed using a composite of carbon black in polydimethylsiloxane (CB PDMS, bulk resistivity of $4.2 \Omega \times \text{cm}$), serves as soft electrical connections to corresponding gold electrodes on the flexible printed circuit board and to conductive hydrogel skin interfaces for ECG. The result is a soft and flexible system (Extended Data Fig. 1b) with applicability across a wide range of settings, focused on, but not limited to, the NICU and PICU (Supplementary Videos 1–3). Robust wireless data transmission and real-time display on a tablet computer is possible across all locations in a standard patient room within an operational range of 10 meters with no measurable heat generation over 24 h of continuous operation (Extended Data Fig. 2a,b).

Power-management schemes. The modular battery unit couples to the device mechanically and electrically through pairs of matching sets of embedded magnets (Fig. 1a, inset), thereby: (1) allowing rapid replacement of the battery to decrease the burden on clinical staff, and to eliminate the risk of skin injury¹⁶; (2) enabling removal of the battery to allow autoclave sterilization of devices (>10 cycles) without measurable changes in operational characteristics; and (3) mechanically decoupling the battery from the device to improve the bendability and, therefore, the compliance at the skin interface. The magnetic scheme also allows other options to be used for power supply, not only in choice of battery size, shape and storage capacity (and therefore operational lifetime), but also in alternative modalities, including battery-free schemes that rely on wireless power transfer (Fig. 1b). As an example of this latter possibility, a magnetically coupled harvesting unit can be configured to receive power from a transmission antenna placed under the bed and designed to operate at a radio frequency of 13.56 MHz with negligible absorption in biological tissue¹⁷. Given that a removable battery can act as a swallowing and choking hazard in older infants, the battery can be designed with geometries that are larger than the minimum size requirements for consumer products used by children (Extended Data Fig. 2c). Figure 1c illustrates a third option, in which a wirelessly rechargeable battery (lithium polymer, 45 mAh) lies within the sealed enclosure of the device to eliminate any external connections. The platform can support tunable operating lifetimes based on the capacity of a battery. Modular coin cells, CR1216 (25 mAh) and CR1632 (120 mAh), can support operation for 2 h and 8 h, respectively. The embedded lithium-polymer rechargeable battery (45 mAh) can support operation for 30 h. The battery-free configuration provides an indefinite lifetime, provided that the device remains in proximity (30–50 cm) of the transmission antenna.

Sensor mechanics and design. The photograph in Fig. 1d features a chest unit deployed on a model of a neonate at an age at which the chance of accidental ingestion is remote, with a small (CR1216, volume = 0.2 cm³), encapsulated button cell as a modular battery. The serpentine interconnects encapsulated with polyimide (PI), the folded configuration and the soft enclosure with gel liner lead to a uniaxial elastic stretchability that exceeds ~33% at the device level, corresponding to an ~500% stretchability in the interconnects prior to encapsulation in the outer silicone shell (Extended Data Fig. 3a,b). The gel (~300 μm thick, ~4 kPa modulus) provides strain isolation between the folded islands to reduce the stresses at the skin interface to levels below the thresholds for sensory perception (20 kPa) for uniaxial stretching of up to 20%, a value at the high end of the range expected in practical use (Fig. 1e and Extended Data Fig. 3c). The resulting elastic bending radius and equivalent bending stiffness are ~20 mm and ~9.6 mm², respectively (Extended Data Fig. 3b). These mechanical characteristics ensure that interfaces with the skin are soft and irritation-free, even in cases of extreme curvatures encountered

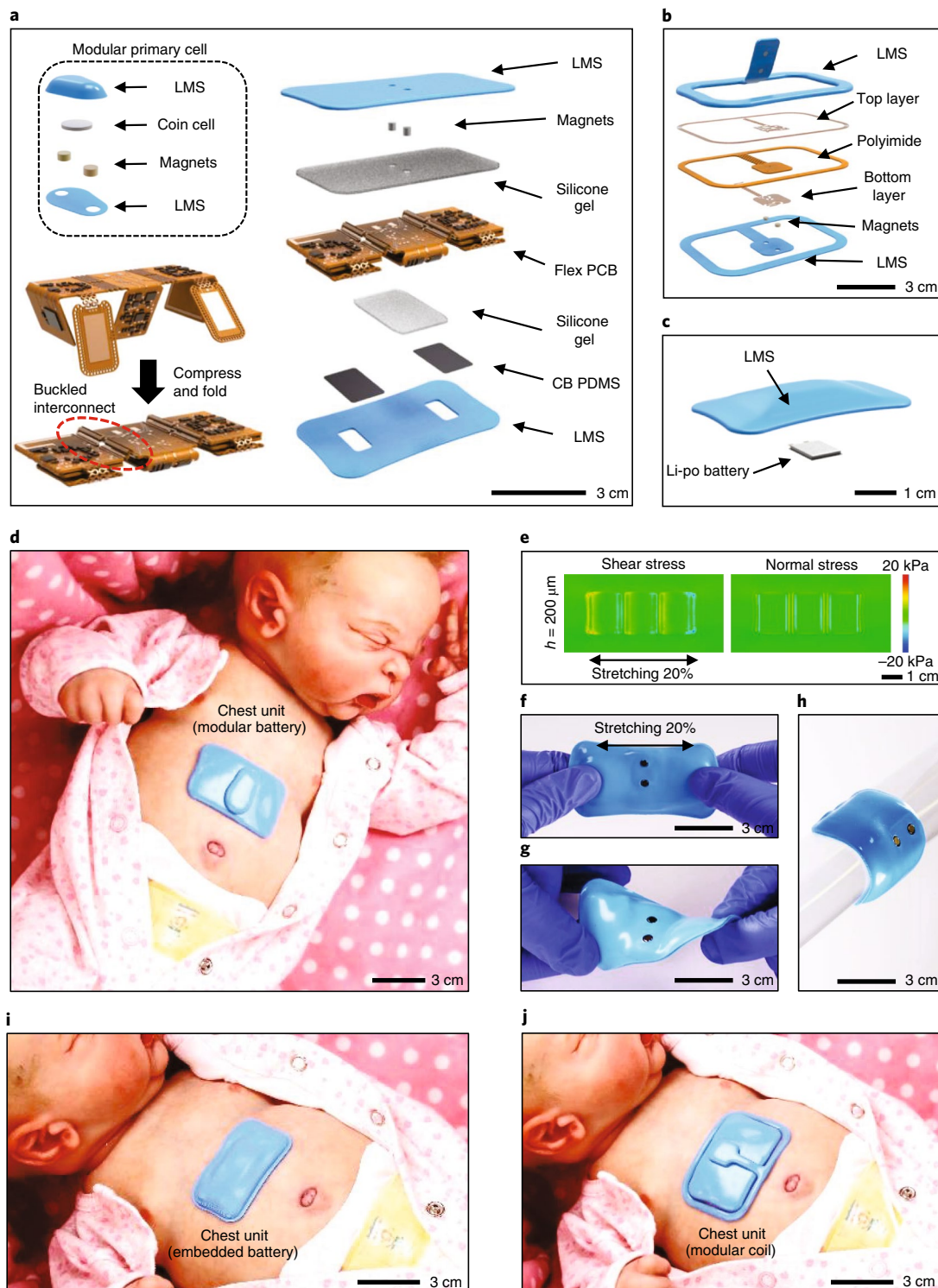


Fig. 1 | Design and characterization of a soft, wireless chest unit for physiological monitoring of neonatal and pediatric patients. **a**, Schematic diagram and exploded-view illustration of a device with a modular primary battery. The main body consists of buckled serpentine interconnects between islands of electrical components contained within a soft, elastomeric enclosure. The battery interfaces to the system via reversible magnetic coupling. Thin conductive silicone pads establish electrical connections between measurement electrodes and a hydrogel interface to the skin. LMS, low-modulus silicone; PCB, printed circuit board. **b**, Illustration of a detachable wireless power-collecting system. **c**, Illustration of a powering option that involves an integrated, wirelessly rechargeable battery. This option is a completely sealed waterproof system that uses a different top-layer encapsulation, without the magnets. **d**, Photograph of the chest unit with a modular battery on a realistic model of a neonate. **e**, Computed stresses (right, normal; left, shear) at the interface between the skin and a chest unit during uniaxial stretching to a strain of 20%, with a chest unit's substrate thickness of 200 μm , defined by h . **f-h**, Photographs of a representative chest unit during stretching (**f**), twisting (**g**) and bending (**h**). **i, j**, Photographs of a chest unit with an embedded battery (**i**) and with a wireless energy harvester (a modular coil) (**j**), both mounted on a model.

with small babies and/or low gestational ages. The images in Fig. 1f–h illustrate a device stretched, twisted and bent to levels that exceed ~20%, ~30° and ~60°, respectively. Mounted units with the embedded battery and battery-free designs appear in Fig. 1i,j.

Figure 2a presents an exploded-view illustration of a device designed to record reflectance-mode photoplethysmograms (PPGs) and skin temperature from peripheral locations that forms the complete monitoring system, together with chest unit. This limb unit features a layout that facilitates wrapping around the foot, palm or toe to accommodate a wide range of ages and anatomies. Figure 2b highlights the overall design, with umbilical interconnects that can bend to radii as small as ~3.9 mm, twist through angles as large as 180° and elastically stretch to uniaxial strains as high as 17% (Extended Data Fig. 3d–h). The fundamental design features are similar to those of the chest unit, but in configurations that anatomically match different limb interfaces: ankle-to-sole of the foot for neonates in the NICU (Fig. 2c) and wrist-to-hand (Fig. 2d) and foot-to-toe (Fig. 2e) for larger pediatric patients in the PICU. In Fig. 2f, we show both chest and limb units deployed on a model of a neonate, along with a representative illustration of vital signs information displayed on a data-logging computer (Supplementary Fig. 1).

Figure 2g presents a block diagram that summarizes the operational scheme. The chest unit includes a wide-bandwidth 3-axial accelerometer (BMI160, Bosch Sensortec), a clinical-grade temperature sensor (MAX30205, Maxim Integrated) and an ECG system that consists of two gold-plated electrodes capped with CB PDMS. The limb unit includes an integrated pulse oximetry module (MAX30101, Maxim Integrated) for measuring dual-wavelength PPGs and a temperature sensor (MAX30205, Maxim Integrated). The power-management circuit for battery operation uses a voltage regulator to provide supply voltages required for the various components (3.3 V or 1.8 V). The modular battery-free platform (Fig. 1b) includes an inductive coil tuned to 13.56 MHz, a full-wave rectifier, and a two-stage cascaded voltage-regulating unit.

Clinical studies on neonatal and pediatric patients in intensive-care units. The soft mechanical properties and the wireless modes of operation are critically important for NICU and PICU patients, particularly when located at highly curved regions of the anatomy and across limited surface areas. Figure 3a,b highlights examples of a chest unit on PICU patients. Figure 3c,d demonstrates use in extremely premature neonates (27 w GA, 6 w chronological age (CA)), also highlighting the option to mount the chest unit on the back of the thorax. Figure 3e–g features the limb unit at various peripheral locations. Wrapping the unit around the ankle-to-base of the foot is effective for premature neonates¹⁸, as are commonly encountered in the NICU. Other options include mounting around the foot-to-toe (Fig. 3f) or the wrist-to-hand (Fig. 3g), typically most suitable for babies with chronological ages greater than 12 months¹⁹. These mounting possibilities enhance nearly all aspects of routine and specialized NICU and PICU procedures, ranging from intimate contact during KC (Fig. 3h) and parental holding to feeding (Fig. 3i), changing diapers (Fig. 3j and Supplementary Fig. 2a) and bathing (Supplementary Fig. 2b).

Real-time measurement of clinical data in the neonatal and pediatric intensive-care unit. Continuous wireless data transmission to a computer system that supports real-time data analytics yields results that can be graphically displayed in an intuitive manner. The chest unit measures ECGs and skin temperature, together with a rich range of information that can be inferred from data collected with the high-bandwidth, three-axis accelerometer, including SCGs, respiration rate and others, with sampling frequencies of 504 Hz (ECG), 0.2 Hz (temperature) and 100 Hz (SCG). The SCG provides information not only on HR, but also on the systolic interval, the pre-ejection period (PEP) and left-ventricular ejection time²⁰. The limb unit measures PPGs at red (660 nm) and infrared (IR, 880 nm) wavelengths, and skin temperature, sampled at 100 and 0.2 Hz, respectively. Figure 4a displays representative ECGs, PPGs, SCGs and chest movements from a neonate with a GA of 29 weeks, captured by continuous wireless streaming to a mobile tablet using the embedded battery version of the platform through gold electrodes (Fig. 1i).

The streamed raw data from the devices pass through the real-time signal-processing algorithm implemented on the mobile tablet, thereby allowing for dynamic, adaptive vital-signs display with negligible time delays (Extended Data Fig. 4). In many cases, relevant information can be extracted from different, independent data streams. For instance, HR can be obtained from ECG (Extended Data Fig. 4a), PPG and SCG data separately to yield multiple, redundant estimations. Similarly, RR can be determined from not only any one of these sources of data, but also from the accelerometry measurements (Extended Data Fig. 4b). Additional opportunities for exploiting redundancy provided by the full multimodal data suite represent topics of current investigation.

Calculation of peripheral capillary oxygen saturation (SpO₂) exploits dual-color PPGs with algorithms designed to minimize the effects of motion artifacts commonly encountered in the NICU and PICU due to naturally occurring movements (Extended Data Fig. 4c). This platform is effective at detecting rapid temporal changes in frequency, as a simple but effective means to reduce motion artifacts^{21,22} (Extended Data Fig. 4d,e).

Figure 4b shows 60 min of HR, SpO₂ and temperature data (see Extended Data Fig. 5a for a magnified plot) obtained from a NICU neonate (GA 29 weeks). These representative data agree well with those captured simultaneously using standard clinical measurements in the intensive-care unit (Intellivue MX800, Philips for HR and SpO₂; Giraffe Omnibed Incubator, GE for temperature; direct physician observation of respiratory rate) with outputs extracted using a licensed software package (BedMaster, Anandic Medical Systems). Direct physician observation serves as the gold standard for respiratory rate, given the known inaccuracies in deriving this parameter in critically ill newborns and children from ECG, PPG or airflow measurements in non-intubated subjects²³. Quantitative comparisons using the Bland–Altman (BA) method²⁴ (Fig. 4c–f) indicate that the mean differences for HR, SpO₂ and temperature are -0.02 beats per minute, 0.11% and 0.21 °C, respectively, for a cohort of $n=3$ patients. The s.d. for HR and temperature are 2.08 beats per minute and 0.26 °C respectively. The accuracy root mean square (A_{rms}) for SpO₂ is 2.99%. The mean difference and the s.d. for RR is 0.11 and 1.95 breaths per minute, respectively for a cohort

Fig. 2 | Designs for a wireless limb unit for physiological monitoring of neonatal and pediatric patients. **a**, Schematic diagram and exploded-view illustration of the limb unit, designed to measure PPG, SpO₂ and peripheral skin temperature. IC, integrated circuit; Li-po, lithium polymer battery. **b**, Photograph of a limb unit that is being bent and twisted. **c–e**, Placement of a limb unit on a model of a neonate at the ankle-to-base of the foot (**c**), on a model of a pediatric patient (2 years old) at the wrist-to-hand (**d**) and on a model of a pediatric patient at the foot-to-toe (**e**). CA, chronological age. **f**, Photograph of the chest and limb units on a model of a neonate in a NICU isolette, with a tablet computer displaying representative data through a graphical user interface. **g**, Block diagram showing the operational scheme of two time-synchronized devices. The chest unit contains an analog-front-end for ECG processing, three-axis accelerometer, thermometer IC and BLE SoC. The limb unit contains a pulse oximeter IC, thermometer IC and BLE SoC. Three different options for power supply are shown at the bottom. ADC, analog-to-digital converter. SPI, serial peripheral interface. I2C, inter-integrated circuit; LED, light-emitting diode; R, red; IR, infrared.

of $n=6$ patients (41 data points). Extended Data Figure 5b presents the global quantitative comparison results, particularly for HR and SpO₂, with 515,679 and 440,077 aggregated data points, respectively, from $n=20$ patients. The results for HR and SpO₂ are

within the regulatory guidelines set by the US FDA, which require errors less than $\pm 10\%$ or ± 5 beats per minute for HR and less than 3.5% for A_{rms} for reflectance mode SpO₂. FDA guidelines for RR monitors under 21 CFR 870.2375 do not specify requirements in





Fig. 3 | Photographs of wireless wearable devices on neonatal and pediatric patients in the NICU and PICU, respectively, and of parental hands-on care with a healthy neonate. a–c, Photographs of the chest unit on two different ~2-year-old children (**a,b**) and on a neonatal preterm infant (27 weeks GA, 6 weeks CA) with apnea of prematurity and respiratory failure (**c**); in this case, the device rests on the back of the infant. **d,e,** Photographs of the limb unit mounted on the ankle-to-foot interface of two infants (27 weeks GA, 6 weeks CA, **d**; and 25 weeks GA, 44 weeks CA, **e**). **f,** Photograph of a similar unit on the foot-to-toe interface of the pediatric patient in **b**. **g,** Photograph of a device on the wrist-to-hand interface of a pediatric patient (35 weeks GA, 6 weeks CA). **h–j,** Photographs of a pair of devices on a 40 weeks GA healthy neonate during KC (**h**), feeding (**i**) and hands-on care (diaper change) (**j**).

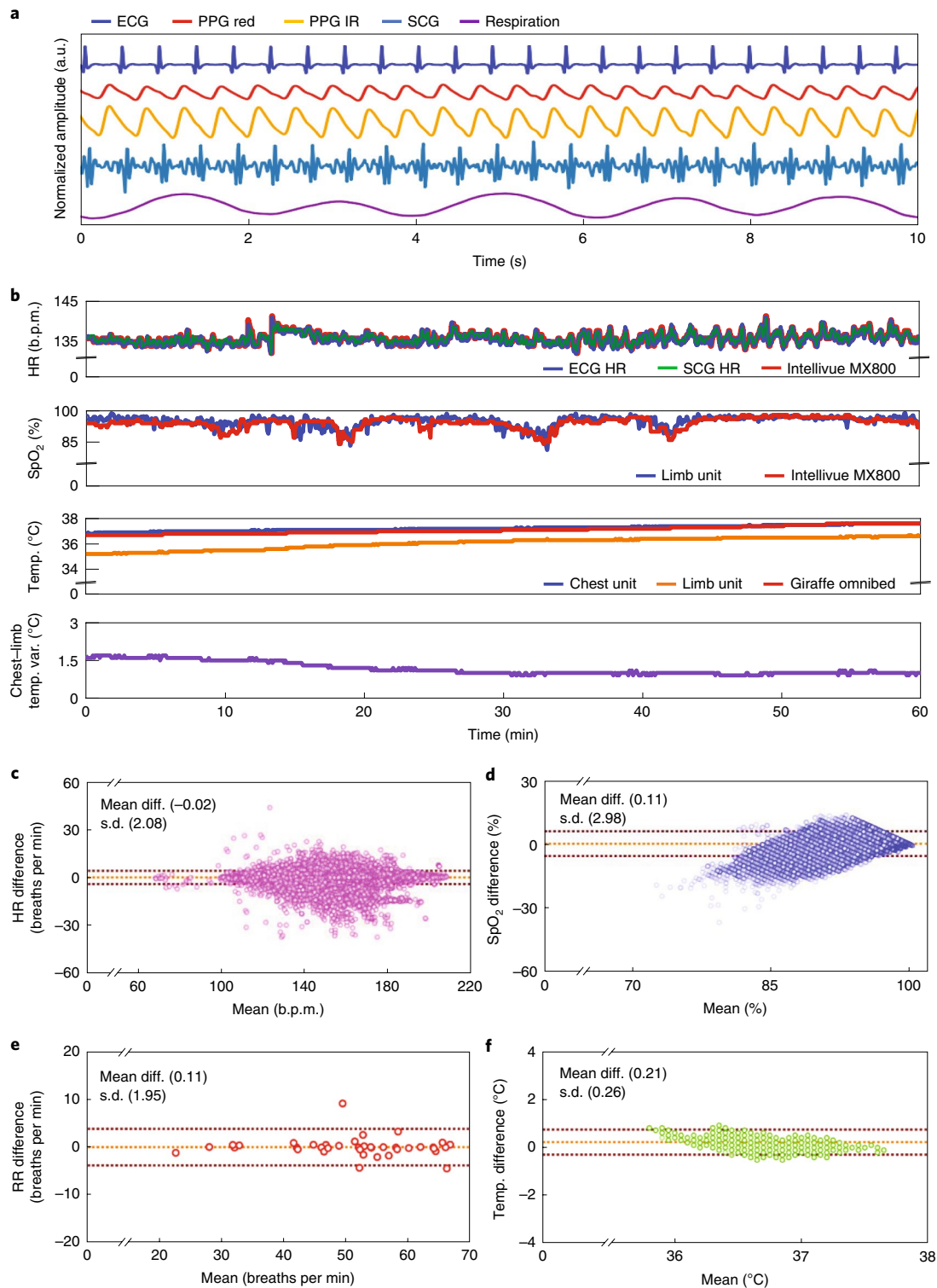


Fig. 4 | Representative data collected in the NICU and PICU by chest and limb units with comparisons to standard measurements. a, Representative ECG, PPG, SCG and respiration waveforms collected from a neonate (29 w GA). ECG and SCG waveforms were collected by a chest unit, while PPG waveforms through both red and infrared LEDs were collected by a limb unit. Respiration is derived by SCG and ECG of a chest unit. **b**, HR, SpO₂, RR, temperature and temperature-gradient data collected from chest or limb units compared with standard clinical measurements in the neonate in **a**. The limb unit was mounted on the foot of the infant. **c–f**, Corresponding Bland-Altman plots to measurement standards for HR from a chest unit (3 subjects, 186,479 data points) (**c**), SpO₂ from a limb unit (3 subjects, 180,913 data points) (**d**), RR from a chest unit (6 subjects, 41 data points) (**e**) and temperature from a chest unit (3 subjects, 15,928 data points) (**f**). Mean diff., mean difference; b.p.m., beats per minute.

terms of accuracy, but previously FDA-cleared bedside monitoring systems target accuracy of ± 3 breaths per minute. Further safety testing on additional neonates ($n=50$) support evaluation of skin

tolerability and ensure negligible heat generation from the sensors operating concomitantly with standard monitoring systems. These results include a diverse range of age groups (23–40 weeks

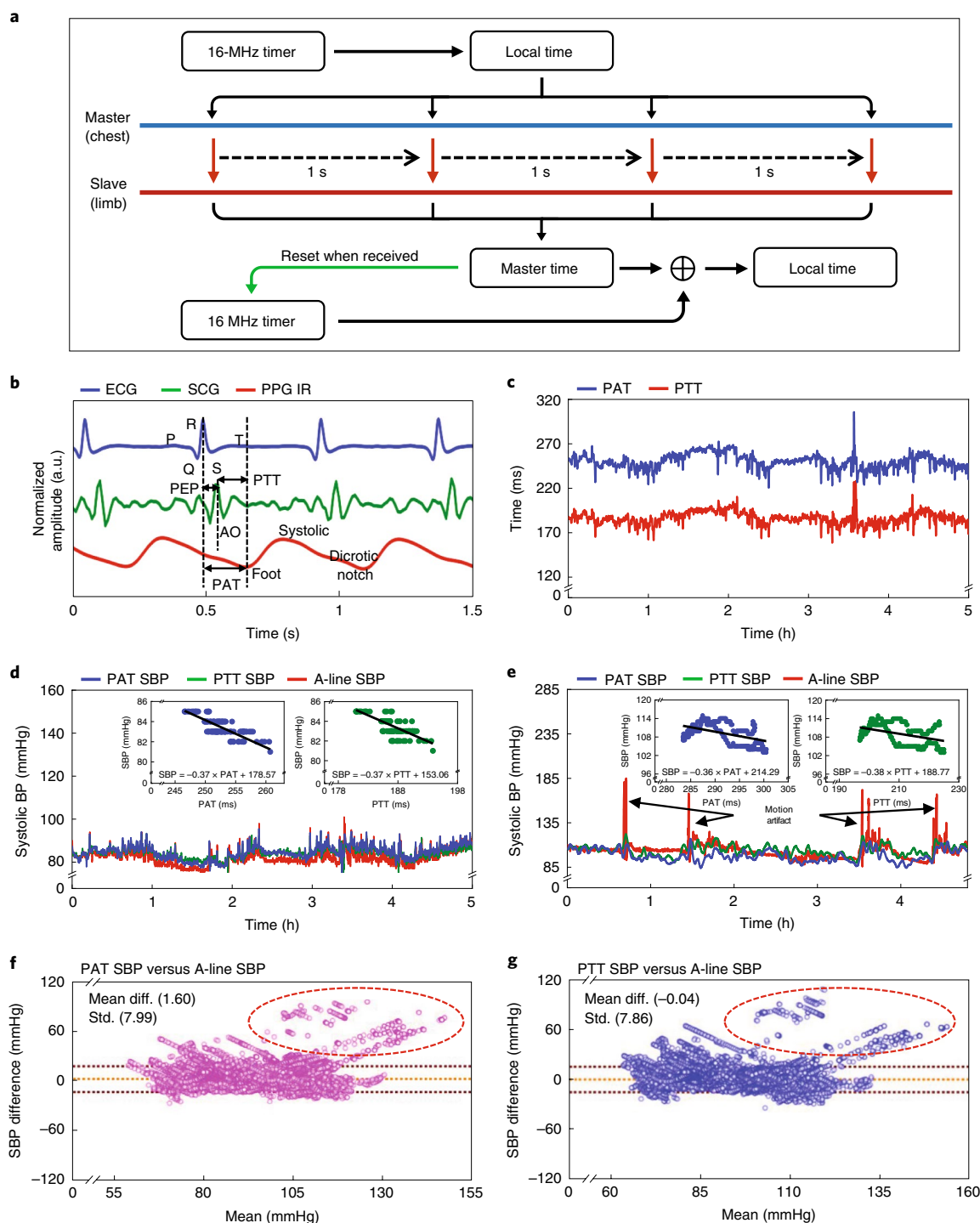


Fig. 5 | Time-synchronized operation of chest and limb units for measurements of systolic blood pressure, with comparison with arterial line data collected from pediatric patients in the PICU. a, Block diagram of the scheme for time synchronization. **b**, Definition of PAT and PTT, as shown in from ECG, SCG and PPG waveforms. AO, aorta opening; P in ECG trace, P wave; QRS in ECG trace, QRS complex; T in ECG trace, T wave. **c**, Representative PAT and PTT data from a pediatric patient in the PICU during a study over the course of 5 h. **d,e**, Systolic blood pressure (SBP) determined on the basis of PAT and PTT measurements, or using an arterial line (A-line) for two infants: (34 weeks GA, 40 weeks CA, **d**; 40 weeks GA, 50 weeks CA, **e**). **f,g**, Bland-Altman plots for PAT-derived SBP ($n=5$ sessions) (**f**) and PTT-derived SBP ($n=5$ sessions) (**g**), as compared with A-line SBP. These plots include data in **d,e**, and Extended Data Figs. 7 and 8. Data points in the red circles correspond to measurement periods in which motion artifacts caused anomalous data from the A-line measurements.

GA and 1 week–4 yr CA), and ethnicities (16 non-Hispanic white, 24 Hispanic/Latino and 10 Black/African American), with no skin adverse events noted, as graded by the Neonatal Skin Condition Score (NSCS)²⁵ (Supplementary Table 1).

Time-synchronized binodal communication for non-invasive blood pressure monitoring. Pulse arrival time (PAT) and pulse transit time (PTT) are two related but distinct measures with established correlations to systolic BP (SBP)²⁶. The PAT, calculated from

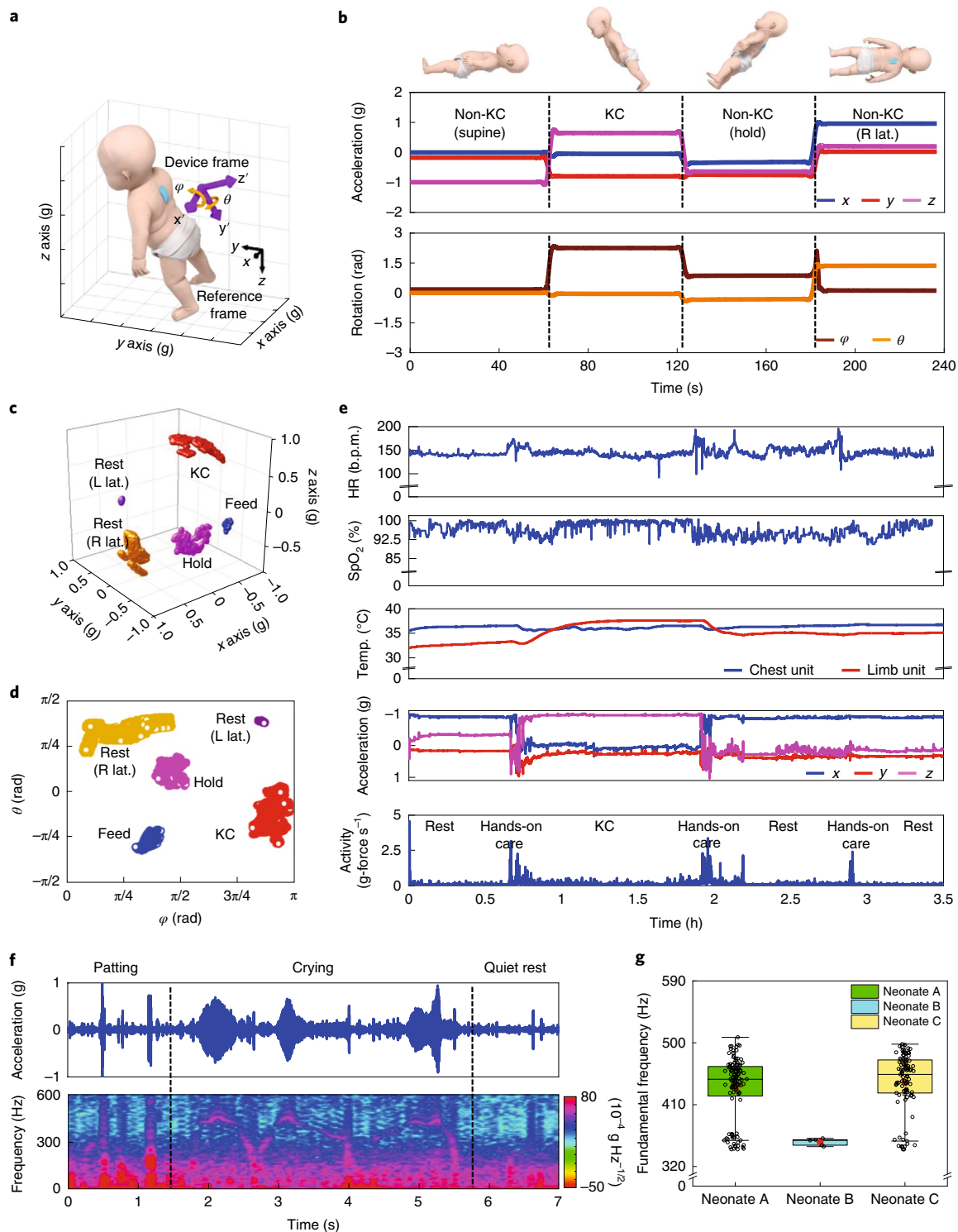


Fig. 6 | Advanced monitoring modalities based on measurements of orientation, activity and vibratory motions. **a**, Definition of the device axes and the rotation angle between the device and reference frames. **b**, Orientation data extracted from low-bandpass filtering of accelerometry data collected from the chest unit, and derived rotation angles for various scenarios: resting in supine and right lateral (R lat.) positions, and non-KC and KC holding. The unit g is defined as the standard acceleration due to gravity ($1g = 9.80665 \text{ m per s}^2$). **c**, Filtered x -, y - and z -axis accelerometry data collected from NICU neonatal patients in various positions. The three-axis accelerometry results quantify the static forces of acceleration on each axis with respect to gravity. **d**, Rotational angles for neonates in NICU in various body positions with respect to the reference frame shown in Fig. 6a ($n = 3$ neonates). **e**, Representative HR, SpO_2 , chest and peripheral-limb temperature, orientation and activity data before, during and after KC with a premature neonate (31 weeks GA). The activity measurement is defined as the root mean square of the three-axes acceleration values between 1 and 10 Hz. **f**, Raw accelerometry signal (top) and spectrogram of time-frequency signal (bottom) during crying and non-crying events recorded from a neonate (37 weeks GA, large for gestational age) with feeding difficulties. Patting involves a gentle and periodic tapping by a caregiver to soothe the neonate. **g**, Fundamental frequency of crying by neonates ($n = 108$ data points for neonate A, 5 for B and 95 for C). The box plot shows the range between the 25th and 75th percentiles. The red dots indicates the mean of each neonate data set. Midline indicates the median. The 3D rendering of the infant image used in **a** and **b** was obtained by TurboSquid as a royalty-free product.

the time difference between the R-peak of ECGs on the chest unit and valley regions of the PPGs on the limb unit, represents the time delay of a pulse pressure wave associated with travel from the aorta to a peripheral limb location for each cardiac cycle. Some studies suggest that the exclusion of the PEP from the PAT may improve correlation with SBP^{27,28}. PTT, calculated from the peak-to-foot time delay between the SCG and PPG waveforms (Fig. 5b), achieves this exclusion by capturing the residual peak when the aorta valve opens. Ultimately, both PAT and PTT depend on vascular system geometry, elasticity, SBP and other factors^{26,29,30}. Extensive studies on adult subjects establish calibrated correlations between PAT, PTT and SBP using both empirical and theoretical models²⁶, some of which are clinically approved for monitoring in certain scenarios (for example, Sotera ViSi Mobile System). Few studies report the correlation of PAT with SBP in infants, mainly in the context of sleep studies and as a screening method rather than a continuous monitoring tool^{31,32}. None report measurements of PTT in critical care populations.

This design integrates synchronous operation of the chest and limb devices, enabling measurements of PAT and PTT for each cardiac cycle. To ensure timing accuracy, once every second, the chest unit transmits its 16 MHz local clock information to the limb unit, as shown in Fig. 5a. The result eliminates timing drift to enable a synchronization accuracy of greater than 1 ms, on average, and a standard deviation of 3.6 ms over a continuous, 24-h period of operation (Extended Data Fig. 6a–c). This scheme requires an additional current consumption of ~0.2 mA compared with the standard mode of operation. The timing interval of one second provides a tradeoff between power consumption and timing accuracy, given that the measured time delays of interest here are typically >100 ms. The proportional model²⁶ derives the linear relationship of PAT and PTT data to SBP, shown in Equation (1), in which PT can represent either PAT or PTT:

$$SBP = -a(PT) + b \quad (1)$$

Calculation of coefficient *a* and constant *b* in this equation involves the linear regression of PAT and PTT data to 5 min of SBP data measured using an A line as an initial calibration. Figure 5c–e shows PAT and PTT data and their linear relationship to SBP collected simultaneously using an A-line from two different infants in the PICU (40 weeks CA and 50 weeks CA, respectively). Accelerometry data from the chest unit (Extended Data Fig. 7a) shows the correlated behavior of the overshoot of the A-line data in Fig. 5e with motion artifact. Such measurements can serve as the basis of a signal-quality index to determine the reliability of the data during motion or other related artifacts. The results show strong agreement throughout the measurement period (Fig. 5d,e). The mean differences of 1.60 and –0.04 mmHg and the s.d. of 7.99 and 7.86 mmHg (Fig. 5f,g) for PAT and PTT-derived SBP values, respectively, indicate their statistical validity (*n* = 5, Extended Data Figs. 7 and 8). The results are within the ANSI/AAMI SP10 standard for labeling, safety and performance requirements for blood-pressure cuffs, which requires a mean difference and s.d. of <5 mmHg and <8 mmHg, respectively. Extended Data Fig. 9 summarizes the effects of calibration for the data of Fig. 5d.

Advanced use cases in kangaroo care and cry analysis. In addition to SCG and PTT, additional clinically important data outputs follow from further use of data from the high-bandwidth three-axis accelerometer. Examples include measuring motion/movement (including tracking KC and holding of the infant), and vocal biomarkers such as tonality, dynamics and frequency of crying. According to guidelines from the World Health Organization (WHO), KC involves holding the neonate in an upright position on the parent's chest, with the neonate's abdomen placed at the level of the parent's

epigastrium, and the neonate's head turned to one side to allow eye contact with the parent³³. This body position, which can be precisely and continuously monitored using low-pass-filtered (0–0.1 Hz) data from the chest-unit accelerometer, is distinct from those that occur during most other activities. Figure 6a presents the device and reference coordinate frames and their relative orientations. Here, Φ and Θ correspond to rotations around the *x* and *y* axis, respectively, consistent with the right-hand rule. Figure 6b demonstrates measurements of core body orientation using data from a chest unit placed on the back of a neonate. Here, a stationary hold in the KC position yields Φ and Θ angles of roughly 2 to 3 rad and –0.5 to 0 rad with respect to the reference frame, respectively. Data collected for the cases of supine, horizontal and right lateral orientations are each significantly different from the KC position ($P < 1 \times 10^{-5}$ for all positions compared with KC) in terms of rotational angle. Figure 6c,d provides 3D representations and angles obtained in the NICU during a KC session. The KC events correspond to 2.85 ± 0.10 rad and -0.29 ± 0.28 rad (data are mean \pm s.d. for 2.4 h) in Φ and Θ , respectively. Comparisons between resting (right and left lateral position), holding, feeding and KC events in this clinical environment each show significant differences in 3-axes acceleration and rotational angle ($P < 1 \times 10^{-5}$, *n* = 3).

Figure 6e highlights the results of HR, SpO₂, central-skin and peripheral-skin temperature, along with a measurement of activity derived from the accelerometry data before, during and after a representative KC study, including removal and return of the neonate to the incubator. Here, activity corresponds to the root mean square value of three-axis accelerometry data after bandpass filtering between 1 and 10 Hz³⁴. The data show that skin-to-skin contact during KC produces a pronounced, gradual increase in the peripheral-skin temperature, consistent with expectation and as demonstrated in previous studies³⁵. The mean activity levels during rest and KC events are 0.07 ± 0.02 g per s, while during hands-on care these values are 0.24 ± 0.05 g per s (data are mean \pm s.d. for 3 neonates, total 8 h of KC or rest and 75 min of hands-on care). These data have the potential to provide quantitative indicators to help minimize the disturbance of neonates during various forms of care, and, therefore, risks of hypopnea, apnea and oxygen desaturation³⁶. Current work seeks to establish methods to use the full set of measurement results to provide feedback on the timing and techniques of KC, particularly in sessions extending beyond 4 h, in which the effects on physiological parameters are expected to be enhanced.

In addition to activity, orientation and SCG, the accelerometer also yields information on vocal biomarkers generally, and crying in particular, via analysis of the high-frequency components of the data. Cry analysis can serve as a non-invasive method to analyze neurophysiological state, often influenced by birth trauma, brain injury, pain, or stress¹³. Crying captured by microphones³⁷ are confounded by ambient sounds in the environment, a particular challenge in NICU and PICU settings. The accelerometer, by contrast, responds only to mechanical vibratory motions of the chest, and is nearly completely unaffected by ambient noise³⁸. Figure 6f shows typical data (top) and the time-frequency signal (bottom) captured at a sampling frequency of 1600 Hz from a neonate. Crying signatures have distinctive frequencies (typically between 400 and 500 Hz, with strong harmonics), well separated from other physiological effects such as cardiac activity (1–50 Hz), muscle tremors (<20 Hz)^{39–41}, or from various operations in care such as patting, rubbing or stroking (Extended Data Fig. 10a–c). Figure 6g summarizes 11 crying events measured in this manner, and in a process of manual recording at the bedside (*n* = 3 infants). The resolution of cry duration from the chest unit was 0.2 s, whereas manual determination of cry duration (manual count) ranged from one second to one minute, dependent on the recorder. The duration of events captured using these two approaches show an average difference of -3.9 ± 13.9 s (data are mean \pm std for 11 cry events) and the

fundamental frequency of 410.7 ± 47.9 is consistent with published results⁴² (Extended Data Fig. 10d).

Discussion

Pilot studies on patients in the NICU and PICU demonstrate the feasibility of a pair of soft, skin-interfaced wireless devices to capture HR, SpO₂ and RR, as well as central-skin and peripheral-skin temperature with high levels of reliability and accuracy as compared with clinical-standard monitoring systems that use conventional, hard-wired interfaces. In fact, the data indicate that in many cases, the wireless operation and the gentle, mechanically stable measurement interfaces reduce the magnitude and prevalence of noise artifacts associated with motions and other parasitic effects that occur during clinical care, feeding, medical imaging and other procedures. In instances of low SpO₂ (<90%), the mean disagreement may reflect different SpO₂ de-noising algorithms rather true differences in measurement—in our patient cohort, subjects were rarely hypoxicemic for a sustained period without medical intervention, such as supplemental oxygen.

In addition to these basic vital signs, time-synchronization techniques yield data that serve as promising surrogates of SBP, thereby offering the potential to bypass the use of blood-pressure cuffs for episodic measurements⁴³ and arterial lines for continuous tracking⁴⁴. Predicate results on adult and pediatric populations lend confidence in the findings presented here, as measurements that exploit accelerometer-based PTT on patients in the NICU and PICU. The device designs and the simplicity of the user interface suggest opportunities for deployment outside of high-resource NICU and PICU facilities and into the developing world and home. The availability of continuous, high-quality data streams at high resolution in these and other contexts may extend the range of utility in both in-patient and remote monitoring.

Another important outcome of the work is in the demonstrated capabilities of the devices to capture advanced and unusual signals, such as SCG, body orientation, activity and vocal biomarkers. Cardiac monitoring with SCG yields important data that complement those associated with ECG, with enhanced utility in early detection of cardiac complications⁴⁵. Although SCG measurements can be performed on adult populations⁴⁶, their use in routine clinical practice is rare, and entirely absent in neonatal and/or pediatric contexts due, at least partly, to the high degrees of curvature of the chest⁴⁷ and the fragility of the skin surface^{48,49}. The same data streams yield, through digital filtering techniques, information on body orientation and activity, which are relevant to identifying and quantifying KC patterns. Quantifying such measures has the potential to provide insight into the role that these activities have in cardiopulmonary status, neurodevelopment and other short- and long-term outcomes⁵⁰. The collective suite of measurements may allow optimization and enhancements in care, in which vital signs and other parameters serve as guiding signatures of efficacy, and as a basis for machine-learning algorithms. Such techniques could offer particular value in the analysis of the neonatal cry as a rich source of information that represents the main natural method for neonates to communicate distress⁵¹. Studies in controlled settings using microphone recordings indicate that cry patterns reflect neurodevelopment and physiological status, with potential relevance to the detection of sudden infant death syndrome⁵², asphyxia, congenital heart diseases and respiratory-distress syndrome⁵³. The platforms introduced here eliminate difficulties associated with ambient alarm sounds in the NICU and PICU, thereby creating an opportunity to exploit this relatively underexplored yet rich source of information³⁷.

Leveraging nursing input, the robust design of these platforms, the options in power supply (Supplementary Fig. 3), the sealed and waterproof construction for devices with the embedded battery option, the soft mechanics, the skin-safe adhesive interfaces with no

instances of skin tearing or dermatitis, the compatibility with established sterilization techniques for devices with the modular battery and wireless power-collecting options, the re-usability of the devices and the alignment of the constituent components, materials and designs with advanced manufacturing practice suggest near term potential for clinical use and broad scalability. The outcomes have the potential to enhance the quality and breadth of neonate information available to physicians, nurses and parents. A growing base of multilateral physiological data, most notably continuous heart activity, respiration, temperature, blood pressure, motion, body orientation and vocal biomarkers, coupled with advanced learning algorithms, may facilitate early diagnosis of many common complications in these populations, including sepsis, seizures and apnea, upon extensive collection and analysis of data from relevant clinical studies⁵⁴. The core technology, beyond neonatal and pediatric critical care, has clear applications in post-acute monitoring, outpatient or home settings, trauma situations and low-resource environments through simultaneous capturing of critical vital signs and new digital biomarkers.

Online content

Any methods, additional references, Nature Research reporting summaries, source data, extended data, supplementary information, acknowledgements, peer review information; details of author contributions and competing interests; and statements of data and code availability are available at <https://doi.org/10.1038/s41591-020-0792-9>.

Received: 24 August 2019; Accepted: 5 February 2020;

Published online: 11 March 2020

References

1. Wheeler, D. S., Wong, H. R. & Shanley, T. P. *Pediatric Critical Care Medicine: Basic Science and Clinical Evidence* (Springer, 2007).
2. Xu, J., Murphy, S. L., Kochanek, K. D., Bastian, B. & Arias, E. Deaths: final data for 2016. *Natl. Vital Stat. Rep.* **67**, 1–76 (2018).
3. Bonner, O., Beardsall, K., Crilly, N. & Lasenby, J. 'There were more wires than him': the potential for wireless patient monitoring in neonatal intensive care. *BMJ Innov.* **3**, 12–18 (2017).
4. Bowdle, T. A. Complications of invasive monitoring. *Anesthesiol. Clin. N. A.* **20**, 571–588 (2002).
5. Cilley, R. Arterial access in infants and children. *Semin. Pediatr. Surg.* **1**, 174–180 (1992).
6. Joseph, R., Chong, A., Teh, M., Wee, A. & Tan, K. Thrombotic complication of umbilical arterial catheterization and its sequelae. *Ann. Acad. Med. Singapore* **14**, 576–582 (1985).
7. Baserga, M. C., Puri, A. & Sola, A. The use of topical nitroglycerin ointment to treat peripheral tissue ischemia secondary to arterial line complications in neonates. *J. Perinatol.* **22**, 416 (2002).
8. Scheer, B., Perel, A. & Pfeiffer, U. J. Clinical review: complications and risk factors of peripheral arterial catheters used for haemodynamic monitoring in anaesthesia and intensive care medicine. *Crit. Care* **6**, 199–204 (2002).
9. Chung, H. U. et al. Binodal, wireless epidermal electronic systems with in-sensor analytics for neonatal intensive care. *Science* **363**, eaau0780 (2019).
10. Fanaroff, J. M. & Fanaroff, A. A. Blood pressure disorders in the neonate: hypotension and hypertension. *Semin. Fetal Neonat. M.* **11**, 174–181 (2006).
11. Wilson, R. A., Bamrah, V. S., Lindsay, J., Schwaiger, M. & Morganroth, J. Diagnostic accuracy of seismocardiography compared with electrocardiography for the anatomic and physiologic diagnosis of coronary artery disease during exercise testing. *Am. J. Cardiol.* **71**, 536–545 (1993).
12. Mahoney, M. C. & Cohen, M. I. Effectiveness of developmental intervention in the neonatal intensive care unit: implications for neonatal physical therapy. *Pediatr. Phys. Ther.* **17**, 194–208 (2005).
13. Shinya, Y., Kawai, M., Niwa, F., Imafuku, M. & Myowa, M. Fundamental frequency variation of neonatal spontaneous crying predicts language acquisition in preterm and term infants. *Front. Psychol.* **8**, 2195 (2017).
14. Boundy, E. O. et al. Kangaroo mother care and neonatal outcomes: a meta-analysis. *Pediatrics* **137**, e20152238 (2016).
15. Dehghani, K., Movahed, Z., Dehghani, H. & Nasiriani, K. A randomized controlled trial of kangaroo mother care versus conventional method on vital signs and arterial oxygen saturation rate in newborns who were hospitalized in neonatal intensive care unit. *J. Clin. Neonatol.* **4**, 26–31 (2015).

16. Shwayder, T. & Akland, T. Neonatal skin barrier: structure, function, and disorders. *Dermatol. Ther.* **18**, 87–103 (2005).
17. Mutashar, S., Hannan, M., Samad, S. & Hussain, A. Analysis and optimization of spiral circular inductive coupling link for bio-implanted applications on air and within human tissue. *Sensors* **14**, 11522–11541 (2014).
18. James, D. K., Dryburgh, E. H. & Chiswick, M. L. Foot length—a new and potentially useful measurement in the neonate. *Arch. Dis. Child.* **54**, 226–230 (1979).
19. Means, L. W. & Walters, R. E. Sex, handedness and asymmetry of hand and foot length. *Neuropsychologia* **20**, 715–719 (1982).
20. Di Rienzo, M. et al. Wearable seismocardiography: towards a beat-by-beat assessment of cardiac mechanics in ambulant subjects. *Auton. Neurosci.* **178**, 50–59 (2013).
21. Leeudomwong, T., Deesudchit, T. & Chinrungrueng, C. Motion-resistant pulse oximetry processing based on time-frequency analysis. *Eng. J.* **21**, 181–196 (2017).
22. Fu, T.-H., Liu, S.-H. & Tang, K.-T. Heart rate extraction from photoplethysmogram waveform using wavelet multi-resolution analysis. *J. Med. Biol. Eng.* **28**, 229–232 (2008).
23. Daw, W. et al. Medical devices for measuring respiratory rate in children: a review. *J. Adv. Biomed. Eng. Technol.* **3**, 21–27 (2016).
24. Bland, J. M. & Altman, D. G. Statistical methods for assessing agreement between two methods of clinical measurement. *Lancet* **327**, 307–310 (1986).
25. Lund, C. H. & Osborne, J. W. Validity and reliability of the neonatal skin condition score. *J. Obstet. Gynecol. Neonatal Nurs.* **33**, 320–327 (2004).
26. Sharma, M. et al. Cuff-Less and continuous blood pressure monitoring: a methodological review. *Technologies* **5**, 21 (2017).
27. Payne, R. A., Symeonides, C. N., Webb, D. J. & Maxwell, S. R. Pulse transit time measured from the ECG: an unreliable marker of beat-to-beat blood pressure. *J. Appl. Physiol.* **100**, 136–141 (2006).
28. Foo, J. Y. A., Lim, C. S. & Wang, P. Evaluation of blood pressure changes using vascular transit time. *Physiol. Meas.* **27**, 685–694 (2006).
29. Peter, L., Noury, N. & Cerny, M. A review of methods for non-invasive and continuous blood pressure monitoring: Pulse transit time method is promising? *IRBM* **35**, 271–282 (2014).
30. Ma, Y. et al. Relation between blood pressure and pulse wave velocity for human arteries. *Proc. Natl Acad. Sci. USA* **115**, 11144–11149 (2018).
31. Wippermann, C. F., Schranz, D. & Huth, R. G. Evaluation of the pulse wave arrival time as a marker for blood pressure changes in critically ill infants and children. *J. Clin. Monit.* **11**, 324–328 (1995).
32. Galland, B. C., Tan, E. & Taylor, B. J. Pulse transit time and blood pressure changes following auditory-evoked subcortical arousal and waking of infants. *Sleep* **30**, 891–897 (2007).
33. World Health Organization. *Kangaroo Mother Care: A Practical Guide* (Department of Reproductive Health and Research, 2003).
34. Liu, G.-Z., Guo, Y.-W., Zhu, Q.-S., Huang, B.-Y. & Wang, L. Estimation of respiration rate from three-dimensional acceleration data based on body sensor network. *Telemed. J. E-Health* **17**, 705–711 (2011).
35. Cattaneo, A. et al. Kangaroo mother care for low birthweight infants: a randomized controlled trial in different settings. *Acta Paediatr.* **87**, 976–985 (1998).
36. Levy, J. et al. Impact of hands-on care on infant sleep in the neonatal intensive care unit. *Pediatr. Pulmonol.* **52**, 84–90 (2017).
37. Reggiannini, B., Sheinkopf, S. J., Silverman, H. F., Li, X. & Lester, B. M. A flexible analysis tool for the quantitative acoustic assessment of infant cry. *J. Speech Lang. Hear. Res.* **56**, 1416–1428 (2013).
38. Liu, Y. et al. Epidermal mechano-acoustic sensing electronics for cardiovascular diagnostics and human-machine interfaces. *Sci. Adv.* **2**, e1601185 (2016).
39. Huntsman, R. J., Lowry, N. J. & Sankaran, K. Nonepileptic motor phenomena in the neonate. *Paediatr. Child Health* **13**, 680–684 (2008).
40. Fahn, S., Jankovic, J. & Hallett, M. in *Principles and Practice of Movement Disorders* 2nd edn (eds Fahn, S., Jankovic, J. & Hallett, M.) Ch. 18 (W.B. Saunders, 2011).
41. Pandia, K., Inan, O.T. & Kovacs, G.T.A. in *2013 35th Annual International Conference of the IEEE Engineering in Medicine and Biology Society (EMBC)* 6881–6884 (2013).
42. Shinya, Y., Kawai, M., Niwa, F. & Myowa-Yamakoshi, M. Preterm birth is associated with an increased fundamental frequency of spontaneous crying in human infants at term-equivalent age. *Biol. Lett.* **10**, pii: 20140350 (2014).
43. Pickering, T. G. et al. Recommendations for blood pressure measurement in humans and experimental animals. *Circulation* **111**, 697–716 (2005).
44. Brzezinski, M., Luisetti, T. & London, M. J. Radial artery cannulation: a comprehensive review of recent anatomic and physiologic investigations. *Anesth. Analg.* **109**, 1763–1781 (2009).
45. Sahoo, P. K., Thakkar, H. K. & Lee, M.-Y. A cardiac early warning system with multi channel SCG and ECG monitoring for mobile health. *Sensors* **17**, 711 (2017).
46. Inan Omer, T. et al. Novel wearable seismocardiography and machine learning algorithms can assess clinical status of heart failure patients. *Circ. Heart. Fail.* **11**, e004313 (2018).
47. Hadush, M. Y., Berhe, A. H. & Medhanyie, A. A. Foot length, chest and head circumference measurements in detection of low birth weight neonates in Mekelle, Ethiopia: a hospital based cross sectional study. *BMC Pediatr.* **17**, 111 (2017).
48. August, D. L., New, K., Ray, R. A. & Kandasamy, Y. Frequency, location and risk factors of neonatal skin injuries from mechanical forces of pressure, friction, shear and stripping: a systematic literature review. *J. Neonatal Nurs.* **24**, 173–180 (2018).
49. Oranges, T., Dini, V. & Romanelli, M. Skin physiology of the neonate and infant: clinical implications. *Adv. Wound Care* **4**, 587–595 (2015).
50. Barbeau, D. Y. & Weiss, M. D. Sleep disturbances in newborns. *Children* **4**, 90 (2017).
51. Newman, J. D. Neural circuits underlying crying and cry responding in mammals. *Behav. Brain Res.* **182**, 155–165 (2007).
52. Corwin, M. J. et al. Newborn acoustic cry characteristics of infants subsequently dying of sudden infant death syndrome. *Pediatrics* **96**, 73–77 (1995).
53. Farsaie Alaie, H., Abou-Abbas, L. & Tadj, C. Cry-based infant pathology classification using GMMs. *Speech Commun.* **77**, 28–52 (2016).
54. Joshi, R. et al. A ballistographic approach for continuous and non-obtrusive monitoring of movement in neonates. *IEEE J. Transl. Eng. Health Med.* **6**, 2700809–2700809 (2018).

Publisher's note Springer Nature remains neutral with regard to jurisdictional claims in published maps and institutional affiliations.

© The Author(s), under exclusive licence to Springer Nature America, Inc. 2020

¹Simpson Querrey Institute, Northwestern University, Chicago, IL, USA. ²Department of Electrical and Computer Engineering, Northwestern University, Evanston, IL, USA. ³Center for Bio-integrated Electronics, Northwestern University, Evanston, IL, USA. ⁴Department of Dermatology, Feinberg School of Medicine, Northwestern University, Chicago, IL, USA. ⁵Department of Materials Science and Engineering, Northwestern University, Evanston, IL, USA. ⁶Division of Pediatric Autonomic Medicine, Department of Pediatrics, Ann & Robert H. Lurie Children's Hospital of Chicago, Chicago, IL, USA. ⁷State Key Laboratory of Structural Analysis for Industrial Equipment, Department of Engineering Mechanics, Dalian University of Technology, Dalian, China. ⁸Department of Biomedical Engineering, Northwestern University, Evanston, IL, USA. ⁹Department of Electrical and Computer Engineering, University of Illinois at Urbana-Champaign, Urbana, IL, USA. ¹⁰Sibel Inc, Evanston, IL, USA. ¹¹Photo-Electronic Hybrids Research Center, Korea Institute of Science and Technology (KIST), Seoul, South Korea. ¹²Department of Mechanical Engineering, Kyung Hee University, Yongin, Republic of Korea. ¹³Frederick Seitz Materials Research Laboratory, University of Illinois at Urbana-Champaign, Urbana, IL, USA. ¹⁴Department of Computer Science, University of Illinois at Urbana-Champaign, Urbana, IL, USA. ¹⁵Department of Mechanical Engineering, Northwestern University, Evanston, IL, USA. ¹⁶Department of Civil and Environmental Engineering, Northwestern University, Evanston, IL, USA. ¹⁷Key Laboratory of C&PC Structures of the Ministry of Education, Southeast University, Nanjing, China. ¹⁸Department of Neurobiology, Northwestern University, Evanston, IL, USA. ¹⁹Department of Biology, Northwestern University, Evanston, IL, USA. ²⁰University of Illinois College of Medicine at Chicago, Chicago, IL, USA. ²¹Department of Graphic Design and Industrial Design at North Carolina State University, Raleigh, NC, USA. ²²Department of Pediatrics, Ann & Robert H. Lurie Children's Hospital of Chicago, Chicago, IL, USA. ²³Division of Neonatology, Department of Pediatrics, Ann & Robert H. Lurie Children's Hospital of Chicago, Chicago, IL, USA. ²⁴Stanley Manne Children's Research Institute, Ann & Robert H. Lurie Children's Hospital of Chicago, Chicago, IL, USA. ²⁵Division of Pediatric Critical Care Medicine, Department of Pediatrics, Ann & Robert H. Lurie Children's Hospital of Chicago, Chicago, IL, USA. ²⁶Department of Chemistry, Northwestern University, Evanston, IL, USA. ²⁷Department of Neurological Surgery, Feinberg School of Medicine, Northwestern University, Chicago, IL, USA. ²⁸These authors contributed equally: Ha Uk Chung, Alina Y. Rwei, Aurélie Hourlier-Fargette, Shuai Xu. ✉e-mail: DWeese-Mayer@luriechildrens.org; jongyoon.lee@sibelhealth.com; jrogers@northwestern.edu

Methods

Fabrication and assembly of the chest and limb devices. FPCB designs using Eagle CAD version 9 (Autodesk), for both the chest and limb sensors. An ISO 9001-compliant PCB manufacturer fabricated the FPCB, followed by a full assembly of components. Programming and folding processes completed the board preparation. For the chest unit with modular options in power supply, films of a soft silicone material (Silbione RTV 4420; part A and part B, mixed with 5% of Silc-Pig silicone opaque dye) formed by spin-casting at 250 r.p.m. and thermal curing (100 °C in an oven for 20 min) on glass slides served as top and a bottom layers for the encapsulation process. A cutting process with a CO₂ laser (ULS) defined openings for the ECG electrodes on the bottom layer and for magnets on the top layer. A silicone-based adhesive (3M 96042) bonded the electronics to the bottom layer. Pre-compression of the serpentine during this step ensured high levels of stretchability, with associated enhancements in the bendability. A silicone gel (Ecoflex, Smooth-On) cured at 100 °C for 20 min provided a soft, strain-isolating interface layer both below (center part) and above (whole coverage) the electronics. Bonding an overlayer of Silbione finalized the encapsulation process. A drop-casting technique formed coatings of Silbione on top of the various modules for power supply.

Fabrication of the integrated secondary battery version of the device exploited a related encapsulation process, but in a design to yield an enclosed air-pocket to minimize the mechanical load associated with the battery. Here, Silbione cast in a machined aluminum mold served as a top capping layer. A film of this same material, formed as previously described, formed a bottom seal at the perimeter region of the shell to complete the enclosure.

An analogous process defined the encapsulation enclosure for the limb unit, with transparent regions at the location of the LED module for PPG measurements. For all devices, a final laser cutting step yielded a smooth, clean perimeter.

A summary of the bill of materials for the chest unit involves passive components (capacitors, inductors and resistors; footprint in inch from 0201 to 0603), power-management units (Bq25120a, Texas Instruments; TPS62740, Texas Instruments), a BLE SoC (nRF52832, Nordic Semiconductor), ECG sensing unit (INA333, Texas Instruments; MAX9638, Maxim Integrated), an inertial measurement unit (BMI160, Bosch Sensortec) and a thermometer unit (MAX30205, Maxim Integrated). The limb device contains passive components (capacitors, inductors and resistors; footprint in inch from 0201 to 0603), power-management units (Bq25120a, Texas Instruments; TPS62740, Texas Instruments), a BLE SoC (nRF52832, Nordic Semiconductor) a PPG sensing unit (MAX30101, Maxim Integrated), and a thermometer unit (MAX30205, Maxim Integrated).

Preparation of soft, integrated electrodes of PDMS doped with carbon black. The formulation involved the addition of 4.5 g of carbon black to 15 g of a silicone prepolymer (Sylgard 184 base) in a 200-ml round-bottom flask containing n-hexanes (100 ml) and vigorous stirring with a stir bar for 10 min at room temperature. Addition of 1.5 g of silicone curing agent (Sylgard 184 curing agent) pre-diluted in 1 ml hexane with continuous stirring for 2–3 min induced polymerization. Rotary evaporation at 40 °C led to simultaneous rapid removal of solvent and degassing of the polymer to yield a smooth paste. Uncured CB-PDMS, spread with a flat edge onto glass slides containing level guides coated with mold-release spray (Ease Release 200, Mann Release Technologies), yielded thin solid films of CB-PDMS (250 μm thickness) after being cured overnight in an oven at 70 °C. Electrode pads, cut with a CO₂ laser to lateral geometries larger by 2 mm along all edges of the openings for the ECG electrodes on the bottom surfaces of the chest unit, provided overlapping regions for bonding. Treatment of both elastomeric surfaces with a corona gun (BD-20A High Frequency Generator, Electro-Technic Products) for 40 s, immediately followed by pressure induced lamination (15 s) and overnight curing at 70 °C in an oven, yielded excellent adhesion. A double-sided conductive tape (3M 9719) bonded the CB-PDMS pads to the gold electrodes on the flexible printed circuit board.

Water immersion tests of the encapsulation structure. Tests of permeation used platforms with the electronic components replaced with a desiccant (Drierite) ($n=4$). Studies involved daily gravimetric measurements following continuous immersion in 1× DPBS at 37 °C. A rapid increase in device weight (>1,000 mg in 24 h) at ~19–28 days followed from partial delamination of the perimeter seal between the top and bottom Silbione layers, as opposed to the seal between the CB-PDMS and Silbione. Additional tests with a functional chest unit with an embedded battery option, continuously immersed in 1× DPBS at 70 °C, demonstrated stable operation, evaluated daily, for 18 d.

Quantifying time-synchronous operation. Characterization of time synchronization used a two-channel function generator to provide a pair of periodic signals (20 ms 3.5 V square pulses separated by 1 s) with a controlled time delay between the two. Connecting one channel to the ECG module and the other to a red LED placed on top of the PPG module yielded data that validated synchronization to a mean delay of less than 1 ms and a standard deviation of 3.6 ms (Supplementary Fig. 10).

Sterilization process. A chest unit with a modular battery option can undergo an autoclave sterilization process through a Heidolph Tuttnauer 3545E Autoclave Sterilizer (Electronic Model AE-K). The process involved a temperature ramp to 121 °C, a sterilization time of 15 min and a drying time of 60 min, performed using a device with the battery removed. Functional tests before and after sterilization revealed no change in performance. Other embedded units underwent the following sensor disinfection procedure, approved by the infection control committee of Ann & Robert H. Lurie Children's Hospital of Chicago.

1. Wash your hands with soap and water before entering the patient's room.
2. Remove the sensors from the patient's skin.
3. Dispose of all hydrogel adhesives in the trash can in the patient's room.
4. Wipe all surfaces of the sensors with a PDI wipe (Sanicloth) continuously for 2 min.
5. Ensure that all surfaces of the sensors remain wet for a full 2 min.
6. Allow the sensors to air dry completely.
7. Wipe all surfaces of the mobile device with a PDI wipe continuously for 2 min.
8. Ensure that all surfaces of the computer remain wet for a full 2 min. Allow the study computer to air dry completely.
9. Before returning the sensors to their containers, inspect the disinfected sensors for visible breaks in the encasing.
10. If there is a visible break in a sensor's encasing, place the sensor in a separate storage container, and return the sensor to the lab to be autoclaved and re-encased.
11. If there are no visible breaks in the sensor's encasing, return the disinfected sensors to their clean container.
12. Wash your hands with soap and water after exiting the patient's room.

Characterizing the temperature sensor. Measurements of the accuracy of the temperature sensor involved immersion in a water bath, heating to 42 °C and then cooling to room temperature, with simultaneous measurements using a reference thermometer (Fisherbrand 13202376, Fisher Scientific) as a standard.

Clinical testing. The research protocol was approved by the Ann & Robert H. Lurie Children's Hospital of Chicago (IRB 2018-1668) and Northwestern University's Institutional Review Board (STU00202449) and was registered on ClinicalTrials.gov (NCT02865070). After informed consent from at least one parent for all participants, the experimental sensors were placed on the chest and limb (foot or hand) by trained research staff. The sensors were placed in a way as to not disrupt any of the existing clinical monitoring equipment. No skin preparation was conducted prior to sensor placement or with sensor removal. The protocol enabled collection times of up to 24 hours. However, medical procedures (for example surgery) or imaging required removal of the sensors. Upon removal of the sensors, a board-certified dermatologist evaluated the underlying skin for evidence of irritation, redness, or erosions. Data were transmitted, collected and stored for further data analysis on a data-logging computer placed out of view of parents and clinical staff. During KC, the parent is dressed in an open-front hospital gown, and the nursing staff facilitates the gentle transfer of the infant to the parent. The infant is rested on the parent's chest in an upright position, head tilted to the side and prone with their legs and arms flexed. This position allows the parent to provide skin-to-skin contact with the infant. The parent is seated for ~1 h, with the infant resting on the parent's chest. All children admitted to the Northwestern Prentice Women's Hospital and Lurie Children's Hospital NICU and PICU were eligible, regardless of gestational age.

The authors affirm that parents or legal guardians of the children included in the study provided written informed consent, for publication of the obscured images in Fig. 3, Supplementary Fig. 2 and Supplementary Video 1.

Data analysis, algorithms and statistics. KC analysis relied on accelerometer measurements captured at a sampling rate of 100 Hz. Calibration involved aligning the x , y and z axes of the device with the gravity vector. Signal processing used a Butterworth low-pass filter (third order) with a cut-off frequency at 0.1 Hz. Simple trigonometry defined the orientation angle from the acceleration values. Results plotted in three dimensions were correlated to manually recorded body positions. Processing the acceleration signal through a Butterworth bandpass filter (third order) between 1–10 Hz, followed by computation of the root mean square of the acceleration values along the x , y and z axes yielded a metric for neonatal activity level, determined each second.

Recording vibratory signatures of vocalization, including crying, involved operation of the accelerometer at a sampling rate of 1,600 Hz. Signal processing used a Butterworth high-pass filter (third order) with a 20-Hz cut-off frequency. Fast Fourier transforms yielded power spectra on time segments with durations of 200 ms. Cry events correspond to spectra with power concentrated between 350 Hz and 500 Hz, with exclusion of harmonics from lower-frequency signals (such as those due to patting).

Statistical analysis was performed with a one-way multivariate analysis of variance (MANOVA) in MATLAB, with an assumption that data points for each group are normally distributed. $P < 0.05$ was considered significant. Collected from more than 20 neonate and pediatric patients, cumulative data points of

515,679 and 440,077 of HR and SpO₂ were used for the comparison analysis between an FDA-approved monitor (Intellivue MX800) and the chest and limb unit, respectively. The difference between the amount of HR and SpO₂ data was caused by multiple factors such as periodic discharge of pulse oximeters following the institution's NICU and PICU protocols. Blood-pressure analysis used 68,048 data points for arterial line-derived SBP and PAT/PTT intervals-derived SBP, collected from 5 neonate and pediatric patients.

Reporting Summary. Further information on research design is available in the Nature Research Reporting Summary linked to this article.

Data availability

All relevant data are included in the paper. Additional supporting data are available from the corresponding authors on request. All request for raw and analyzed data and materials will be reviewed by the corresponding authors to verify whether the request is subject to any intellectual property or confidentiality obligations. Patient-related data not included in the paper were generated as part of clinical trials and may be subject to patient confidentiality. Source data for Figs. 4–6 and Extended Data Figs. 2, 4, 5 and 7–10 are presented within the paper.

Acknowledgements

D.E.W.-M., A.H., C.M.R., R.G. and J.A.R. acknowledge funding from the Bill & Melinda Gates Foundation (OPP1182909). S.X. and J.A.R. acknowledge additional funding from the Bill & Melinda Gates Foundation (OPP1193311). D.E.W.-M., A.H., C.M.R., R.G. and J.A.R. acknowledge support from the Gerber Foundation. A.S.P., D.E.W.-M., A.H. and J.A.R. recognize the Friends of Prentice Foundation for their support. J.A.R. and S.X. also recognize support from Save the Children (award 999002170). A.Y.R. gratefully acknowledges funding support by the National Institutes of Health's National Center for Advancing Translational Sciences, grant TL1TR001423. The content is solely the responsibility of the authors and does not necessarily represent the official views of the National Institutes of Health. E.S. recognizes funding support from the WCAS Undergraduate Research Grant Program, which is administered by Northwestern University's Weinberg College of Arts and Sciences. The conclusions, opinions and other statements in this publication are the author's and not necessarily those of the sponsoring institution. This work is also supported by the National Natural Science Foundation of China (11402134 and 11320101001), the National Basic Research program of China (2015CB351900) and the National Science Foundation (1400159, 1534120 and 1635443). The materials and engineering efforts were supported by the Center for Bio-Integrated Electronics of the Simpson Querrey Institute at Northwestern University. This work

utilized Northwestern University Micro/Nano Fabrication Facility (NUFAB), which is partially supported by Soft and Hybrid Nanotechnology Experimental (SHyNE) Resource (NSF ECCS-1542205), the Materials Research Science and Engineering Center (DMR-1720139), the State of Illinois and Northwestern University.

Author contributions

A.S.P., S.X., D.E.W.-M., A.H., Y.H. and J.A.R. conducted the overall research program; H.U.C., A.Y.R., A.H.F., K.H.L., C.L., A.C., E.K., J.C., I.C.O., K.B.F., A.B., Jongwon Kim, H.J., M.N., J.W.K., E.S., M.A.P., R.J.K., B.V.P., K.A.H., M.P., H.S.K., S.H.L., J.D.L., Y.Y., S.R., T.S., I.J. and H.A. performed and were involved in the manufacturing of the sensors; H.U.C., A.Y.R., A.H.F., K.H.L., Z.X., C.L., D.R., E.K., J.C., W.R. and J.Y.L. were responsible for the overall engineering design of the sensors; H.U.C., A.Y.R., A.H.F., D.H.K., D.R., C.O., D.G., M.I., A.B. and J.Y.L. were responsible for data analysis; E.C.D., B.H., V.R.S., A.O., A.S., A.B., M.S., C.M.R., L.E.M., Z.L.H., A.H., A.S.P., D.E.W.-M. and S.X. were responsible for data collection; Z.X., K.H.L., R.A., Y.X. and Y.H. performed the mechanical and structural design; H.U.C., D.H.K., D.R., C.O., D.G., J.B.P., J.L., Y.P., Jungwoo Kim, H.H.J., H.H., S.S.K., M.I. and J.Y.L. performed software design, software validation, signal processing and algorithm development; A.S.P., D.E.W.-M., C.M.R., S.X. and J.A.R. were responsible for acquiring funding; H.U.C., A.R., A.H.-F., S.X., J.Y.L. and J.A.R. wrote the original draft of the manuscript; and all authors participated in editing and reviewing of the final manuscript.

Competing interests

H.U.C., S.X., D.H.K., D.R., E.K., J.C., A.B., J.B.P., J.L., J.K., H.H.J., S.S.K., J.D.L., J.Y.L. and J.A.R. declare equity ownership in a company that is pursuing commercialization of the technology described here.

Additional information

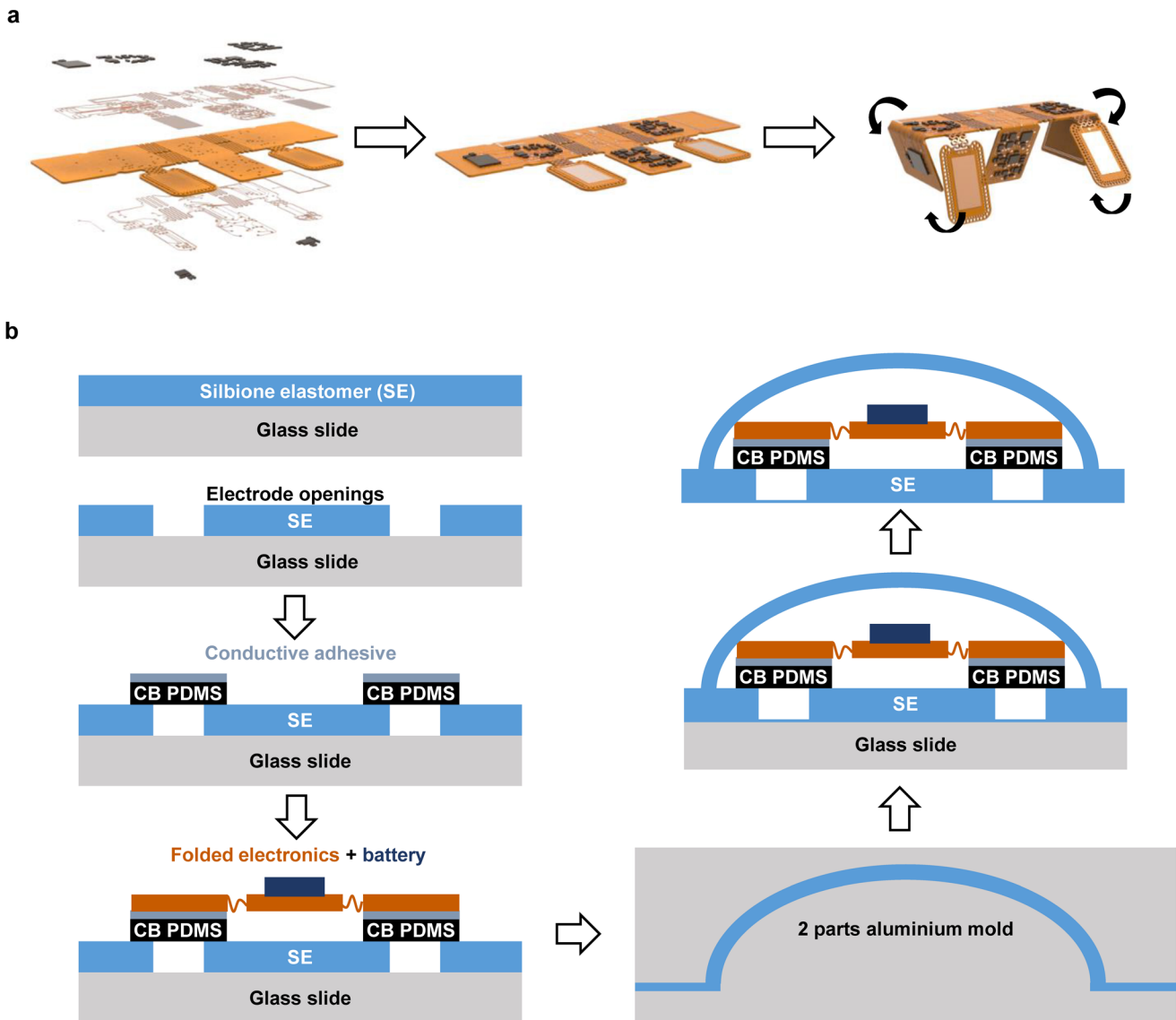
Extended data is available for this paper at <https://doi.org/10.1038/s41591-020-0792-9>.

Supplementary information is available for this paper at <https://doi.org/10.1038/s41591-020-0792-9>.

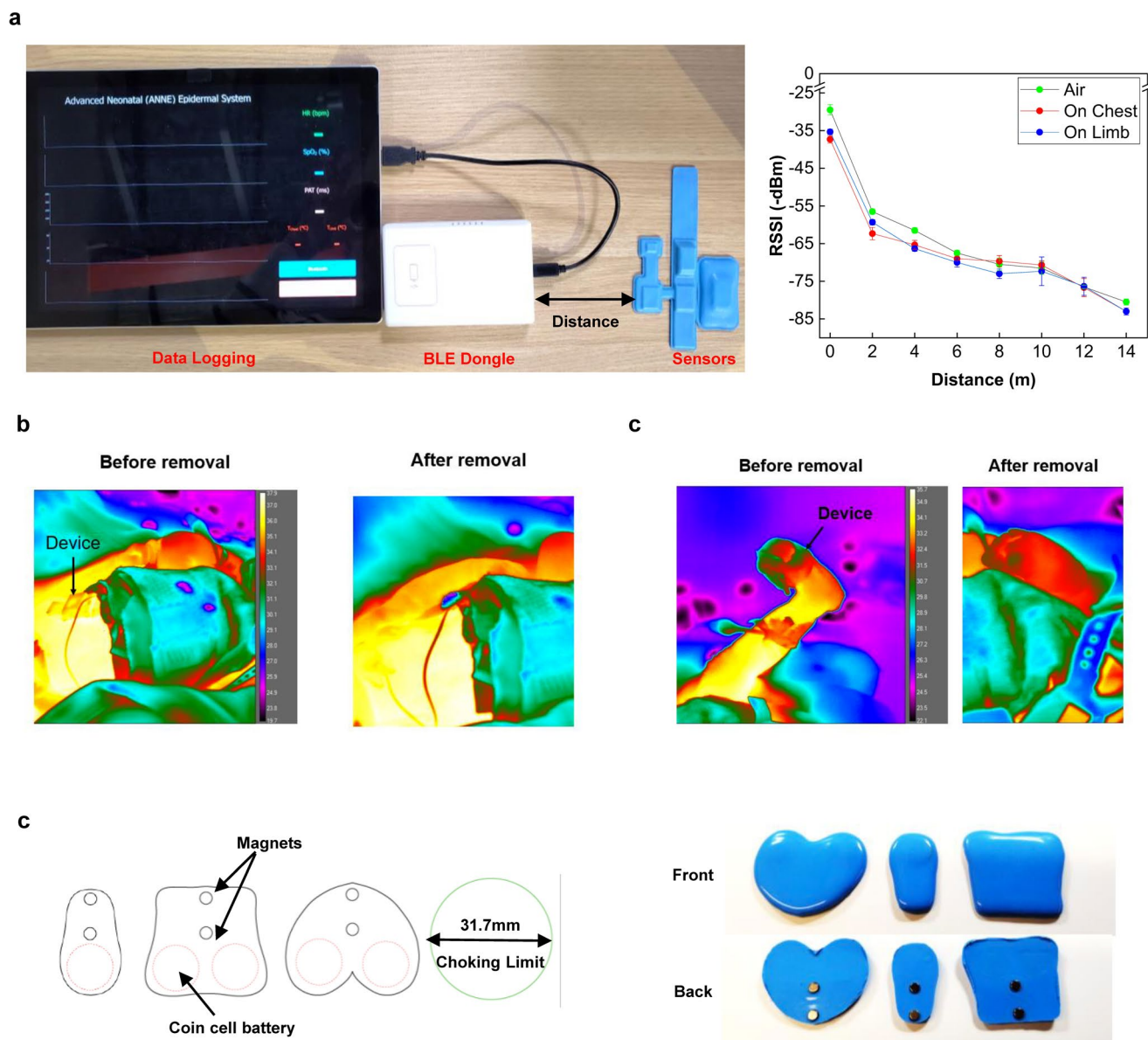
Correspondence and requests for materials should be addressed to D.E.W.-M., J.Y.L. or J.A.R.

Peer review information Michael Basson was the primary editor on this article and managed its editorial process and peer review in collaboration with the rest of the editorial team.

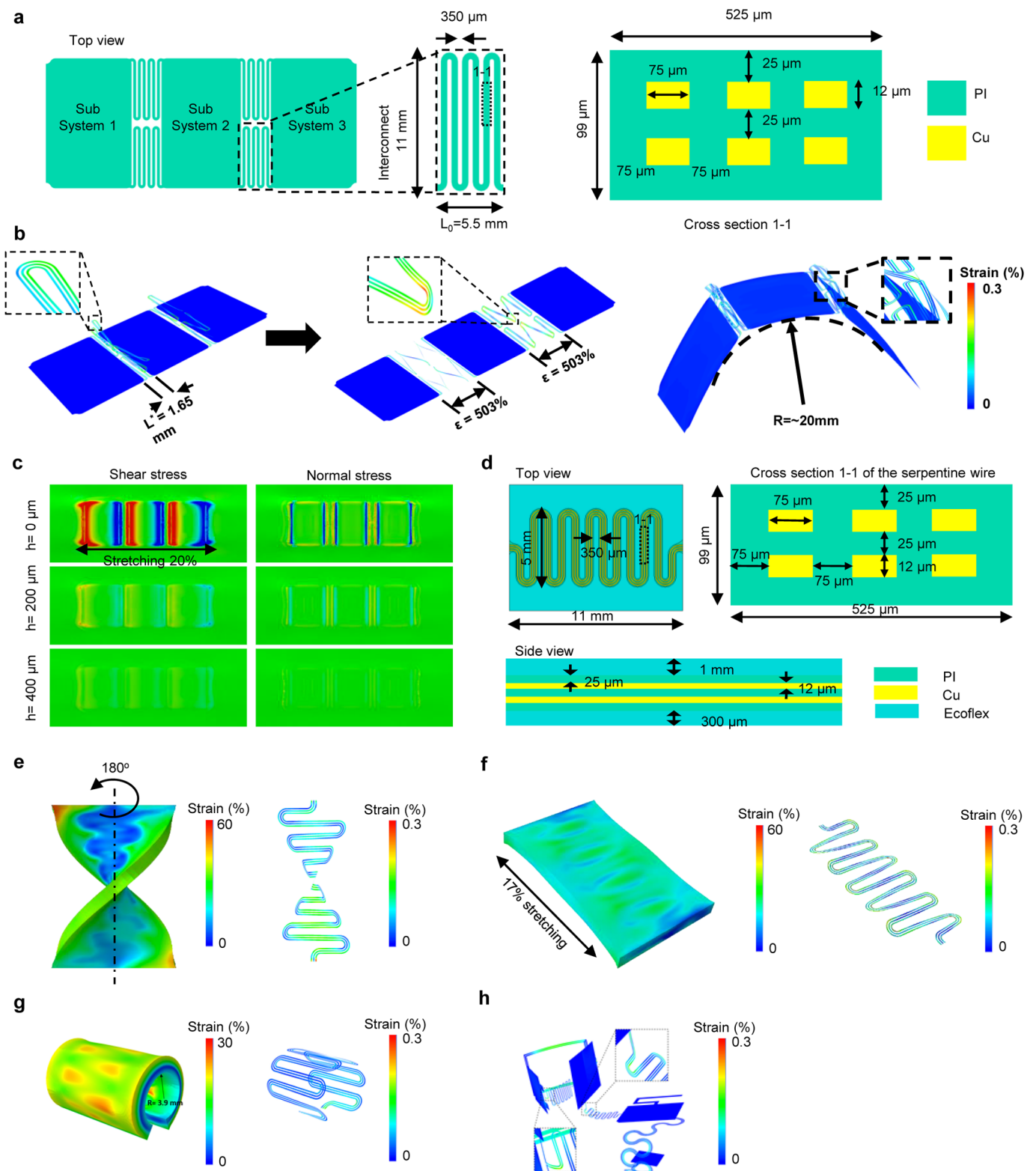
Reprints and permissions information is available at www.nature.com/reprints.



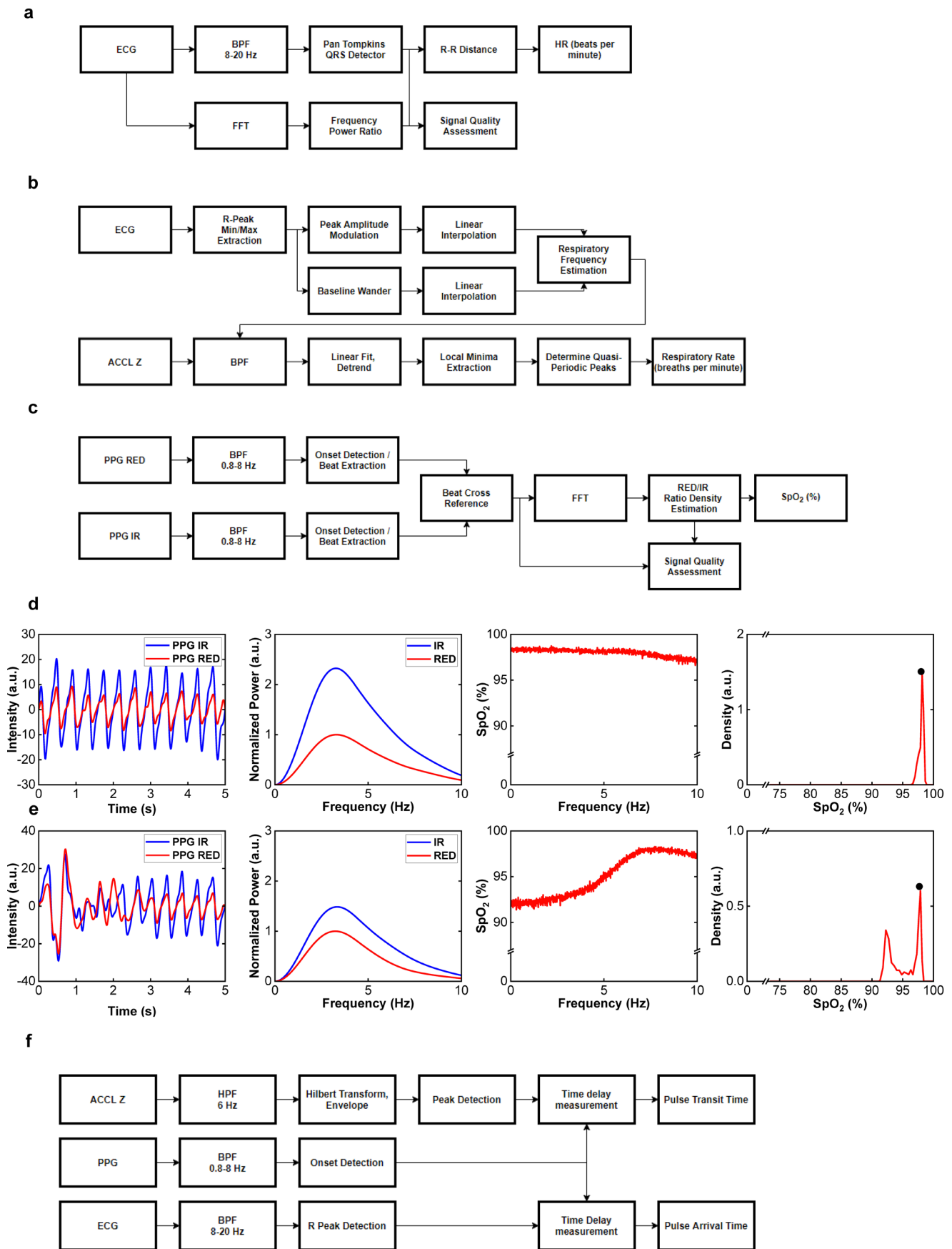
Extended Data Fig. 1 | Fabrication Process of a Chest unit. **a**, Leftmost and middle diagrams show the assembly process of the circuit components on a 2-layer flexible printed circuit board. Rightmost diagram shows how the sub-systems of the chest board are folded. **b**, The encapsulation process involves spin casting Silbione elastomer on top of a glass slide, followed by opening for the electrodes. CB PDMS is used to fill the electrode openings, then combined with the folded board that contains a battery. The top Silbione enclosure is prepared through a 2-part molding process and closes the encapsulation of the chest unit. Removing the glass slide finalizes this process. CB PDMS, carbon black in polydimethylsiloxane.



Extended Data Fig. 2 | Information on connectivity, thermal safety, and modular batteries. **a**, Measurement of connectivity between sensors and base station (connected with a BLE dongle) involves a received signal strength indicator (RSSI). RSSI was measured at a distance between sensors and the base station from 0 to 14 meters (incremental of 2 meters) three times at three different cases when 1) the chest unit in air, 2) the chest unit was on a healthy adult's chest, and 3) the limb unit on the finger of the same person. Standard deviation between three measures at every distance is defined as the error bar in the plot. BLE, Bluetooth Low Energy. **b**, Representative pictures showing temperature changes on a subject's chest when a chest unit is mounted, operational for 24 hours. Negligible change was observed ($n = 3$). **c**, Similarly, negligible change in temperature was observed, when a limb unit was mounted on the foot of the same subject for 24 hours in full operation ($n = 3$). **d**, Different form factors of encapsulated modular batteries. The green colored circle with the diameter of choking limit outlines the safety limits to prevent choking hazard for kids under 3 years old.

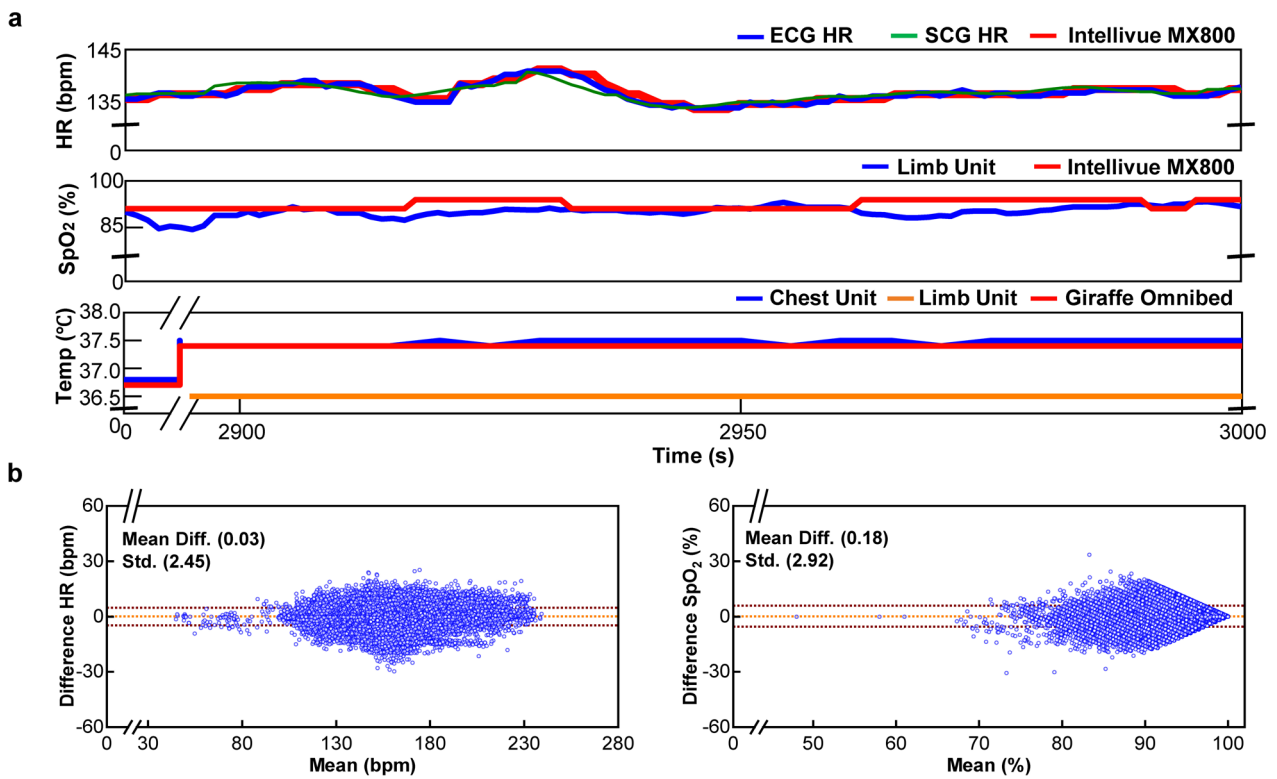


Extended Data Fig. 3 | Mechanical properties of chest and limb units. **a**, Schematic illustration of stack and dimension information for serpentine interconnects and sub-systems of a chest unit. PI, polyimide. Cu, copper. **b**, Computational result showing the stretchability and bendability of a chest unit's board. L_0 , nominal length of a serpentine interconnect of the board. L^* , pre-compressed length of the serpentine. $\epsilon = (L - L^*) / L^*$ defines the elastic stretchability. **c**, Computational result showing the effect of thickness of the strain isolation layer regarding shear and normal stress when a chest board is assumed to be stretched by 20%. **d**, Schematic illustration of the stack and dimension information for serpentine interconnects of a limb unit. **e**, Strain distribution in the encapsulation layer (left) and copper layer (right) of an interconnect during (**e**) twisting, (**f**) stretching, (**g**) and bending at the radius of 3.9 mm. **h**, Overall bending mechanics of a limb unit board illustrated by strain distribution.

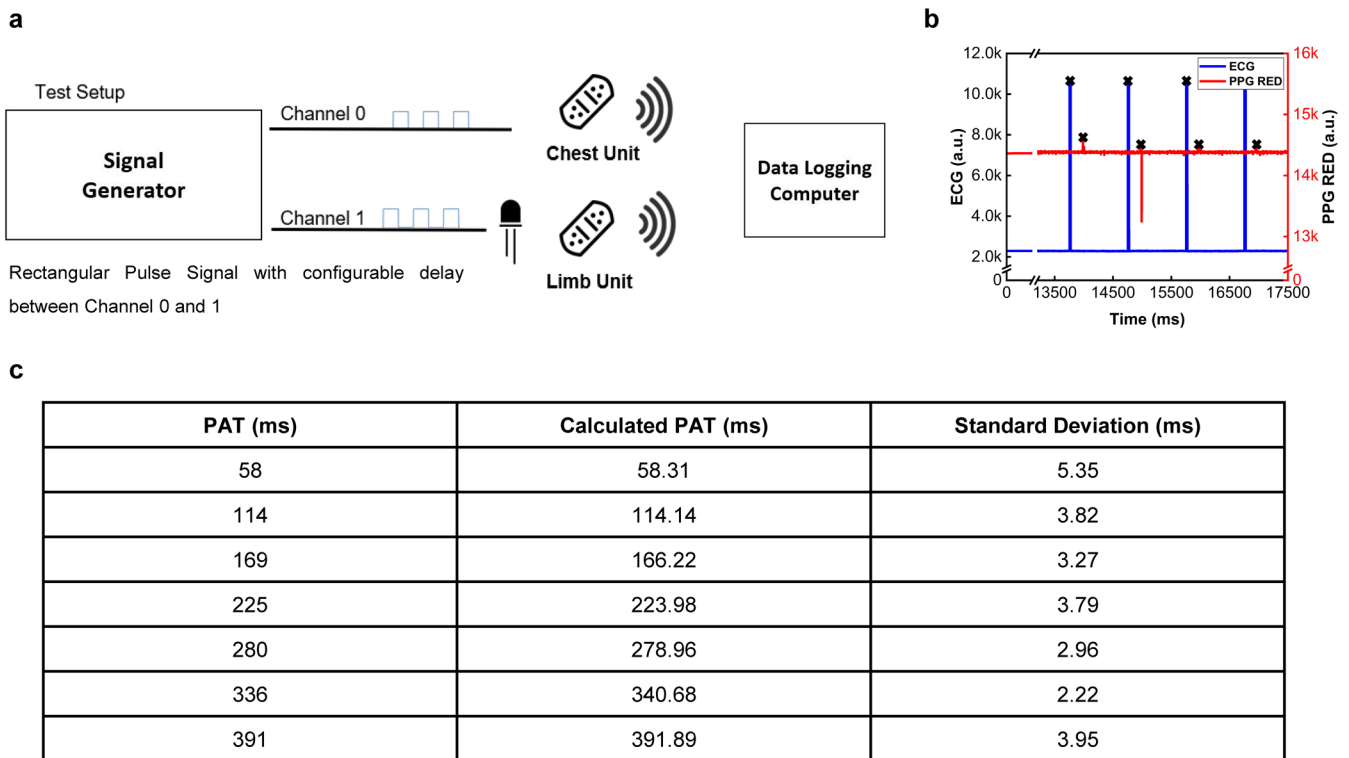


Extended Data Fig. 4 | See next page for caption.

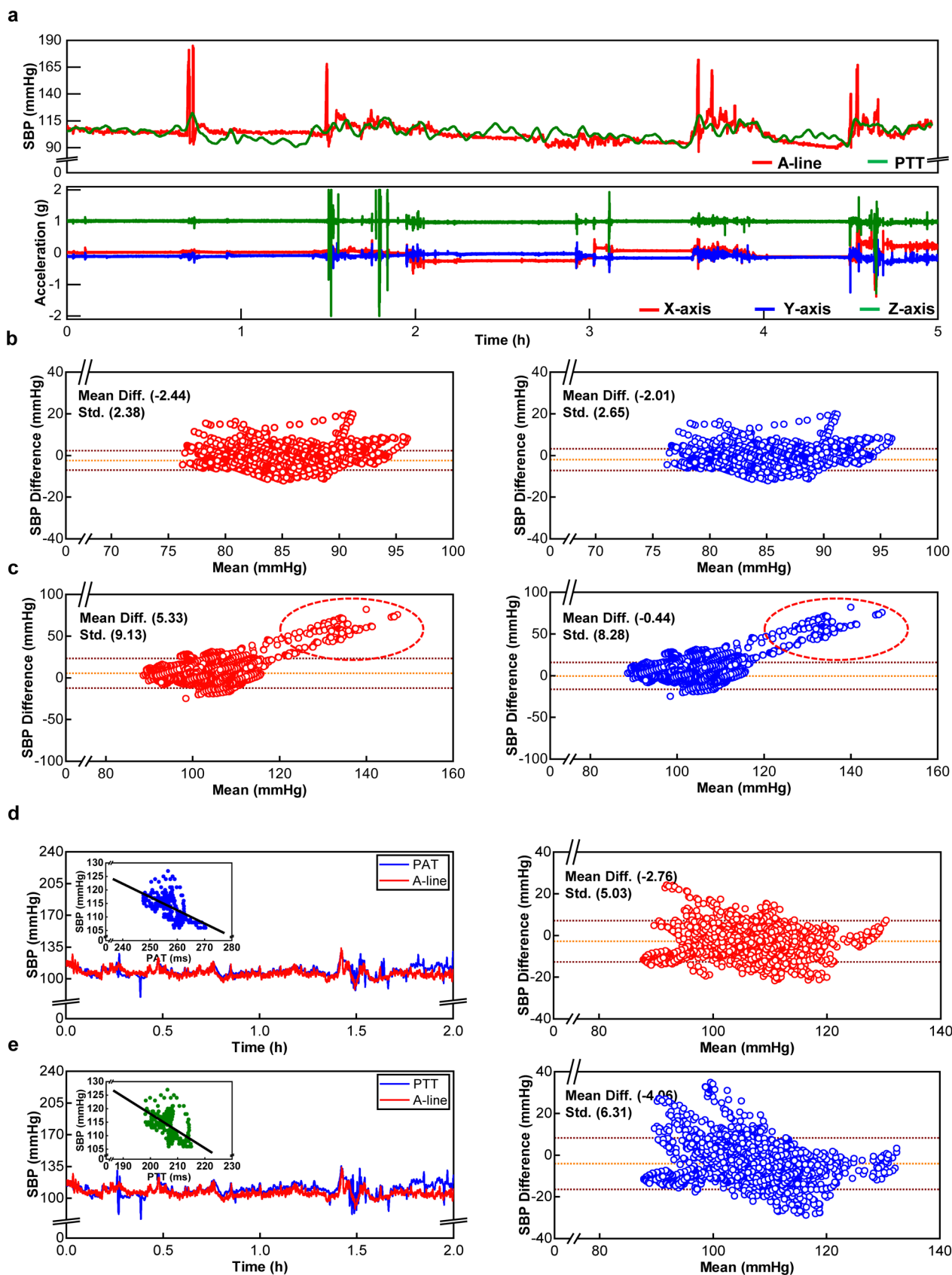
Extended Data Fig. 4 | Vital signs processing algorithm. Block diagram of the signal processing algorithm for (a) heart rate, (b) respiration rate, (c) SpO₂. d,e, representative images showing differences between sub-processed time-domain and frequency-domain responses for the signal (d) without motion artifact and (e) with motion artifact. f, Block diagram of signal processing algorithm for pulse timing calculations. BPF, bandpass filter. ECG, electrocardiogram. QRS, QRS complex of ECG. R-R distance, distance between two consecutive R-peaks of ECG. ACCL, acceleration output. PPG, photoplethysmogram output. IR, infra-red.



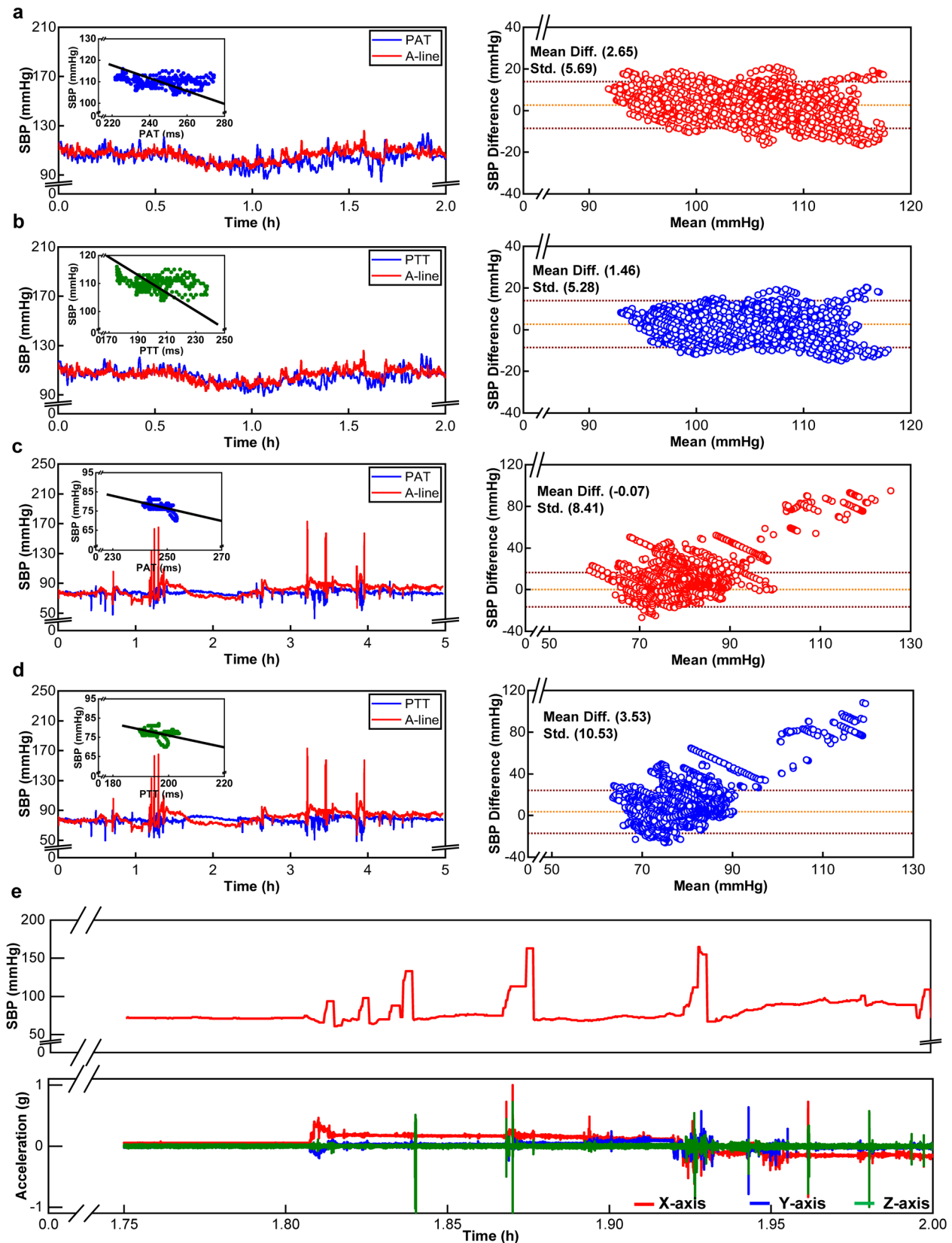
Extended Data Fig. 5 | Vital signs comparison of sensors to FDA-cleared equipment. **a**, Closed view around 100 seconds of HR, SpO₂, and Temperature plots in Fig. 4b. Global Bland Altman plots for **b**, HR (n = 515,679 from 20 NICU and PICU subjects) and **c**, SpO₂ (n = 440,077 from 20 NICU and PICU subjects).



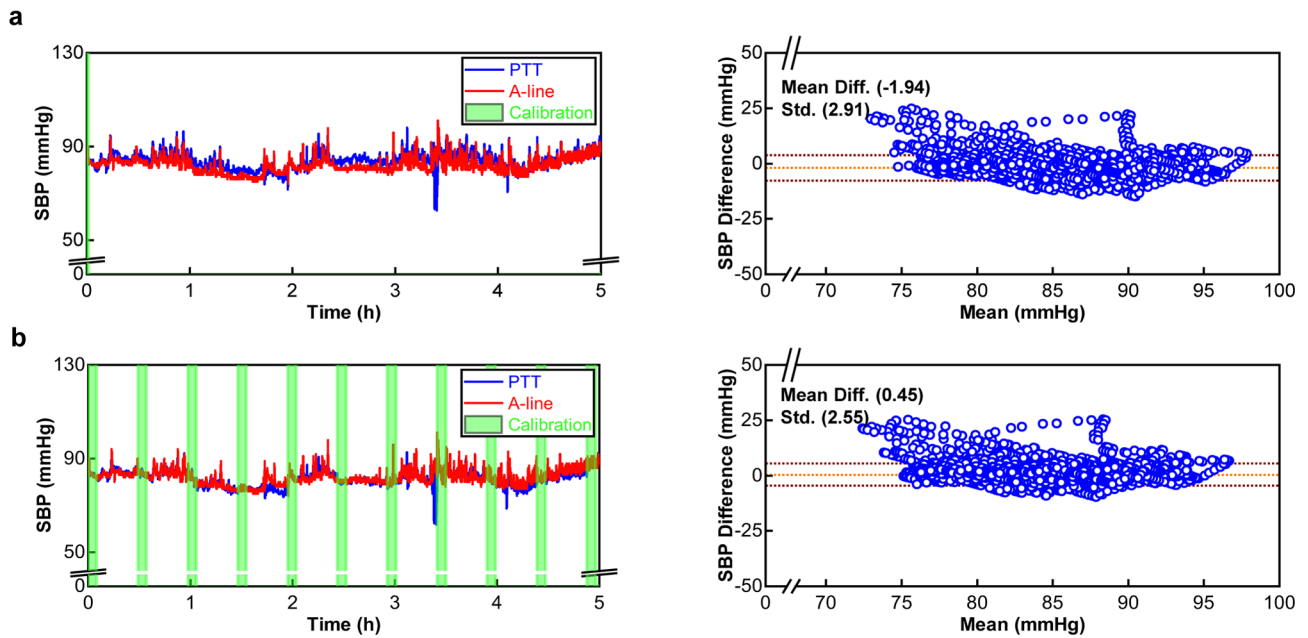
Extended Data Fig. 6 | Time-synchronization verification experiment for the sensors. **a**, Testing set up involves a signal generator sending rectangular pulses to a chest unit, while received data is streamed over to the base station. The signal generator sends a delayed signal to switch the Red LED and the photodetector in the limb unit to capture the output associated with LED switching, followed by streaming the output to the same base station. **b**, A representative plot showing two signals obtained from the chest and limb unit with a delay between two units defined by the signal generator. **c**, Mean and standard deviation of calculated timing difference compared to defined delay (testing PAT).



Extended Data Fig. 7 | Analysis of estimating blood pressure using pulse timing parameters. **a**, A representative plot showing large movement in accelerometry data (bottom) correlates to large and sudden changes in arterial line (A-line) derived SBP signal (top). Bland Altman plots of PAT- and PTT-derived SBP compared to A-line SBP from the data shown in **b**, Fig. 5d ($n = 18,679$ data points for both left and right), **c**, Fig. 5e ($n = 17,449$ data points for both). **d**, A plot (left) of A-line SBP (red) and PAT SBP (blue) and the resulting Bland Altman plot (right, $n = 7,322$ data points) for the subject with H/O splenectomy (39 w GA, 95 w CA). **e**, A plot (left) of A-line SBP (red) and PTT SBP (blue) and the resulting Bland Altman plot (right) for the same subject ($n = 7,322$ data points).

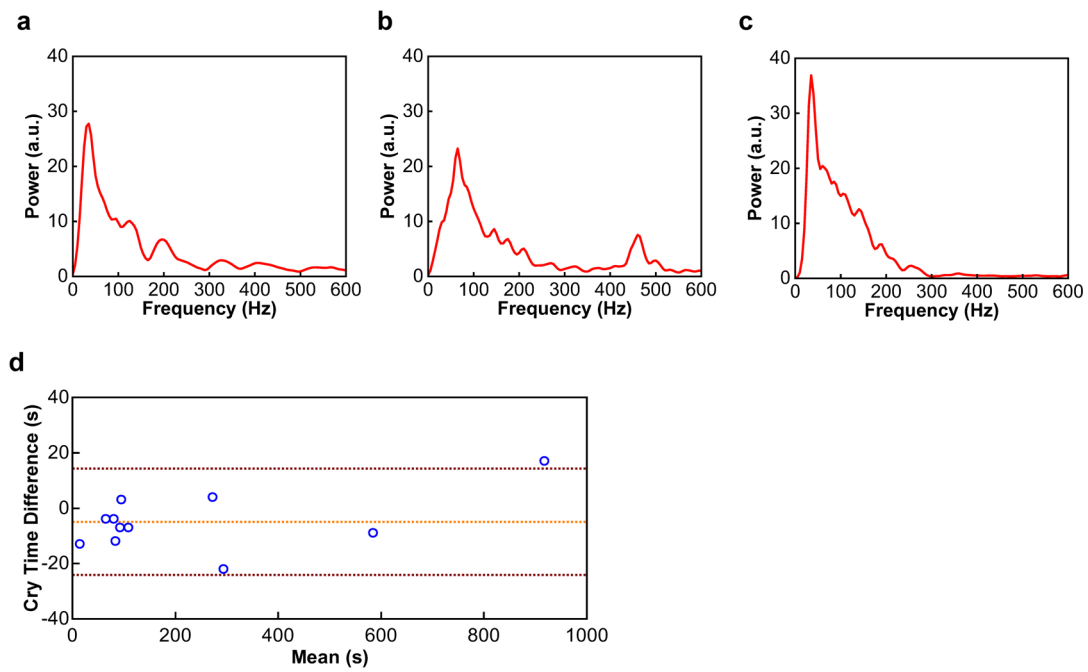


Extended Data Fig. 8 | Analysis of estimating blood pressure using pulse timing parameters. **a**, A plot (left) of A-line SBP (red) and PAT SBP (blue) and the resulting Bland Altman plot (right) for the same subject in ED Fig. 7 ($n = 7,024$ data points). **b**, A plot (left) of A-line SBP (red) and PTT SBP (blue) and the resulting Bland Altman plot (right) for the same subject in (a), ($n = 7,024$ data points). **c**, A plot (left) of A-line SBP (red) and PAT SBP (blue) and the resulting Bland Altman plot (right), ($n = 17,514$ data points) for the subject with hypoxia and hypercapnia (40 w GA, 69 w CA). **d**, A plot (left) of A-line SBP (red) and PTT SBP (blue) and the resulting Bland Altman plot (right) for the same subject ($n = 17,514$ data points). **e**, Accelerometry analysis to verify correlation between large spikes in A-line SBP (top) and motion artifact (bottom).



Extended Data Fig. 9 | The effect of calibration window size and re-calibration period in estimating blood pressure using pulse timing parameters.

a, A plot (left) of A-line SBP vs PTT SBP obtained from the same subject in Fig. 5d and its resulting Bland Altman plot (right, $n = 18,979$ data points) with a single calibration was applied in the first minute of data. **b**, A plot (left) of A-line SBP vs PTT SBP of the same subject in (a) and its resulting Bland Altman plot (right, $n = 18,739$ data points) while having calibration every 30 minutes with a calibration window size of 5 minutes.



Extended Data Fig. 10 | Accelerometry for analyzing characteristics of crying by a chest unit on neonates. Representative power spectrum of signal frequency upon fast Fourier transform processing of neonatal mechano-acoustic signal during **a**, patting, **b**, resting, and **c**, crying. **d**, Bland Altman plot for comparison between cry duration calculated by a chest unit's data and manual recording ($n = 11$ data points from 3 neonates).

Reporting Summary

Nature Research wishes to improve the reproducibility of the work that we publish. This form provides structure for consistency and transparency in reporting. For further information on Nature Research policies, see [Authors & Referees](#) and the [Editorial Policy Checklist](#).

Statistics

For all statistical analyses, confirm that the following items are present in the figure legend, table legend, main text, or Methods section.

n/a Confirmed

- The exact sample size (n) for each experimental group/condition, given as a discrete number and unit of measurement
- A statement on whether measurements were taken from distinct samples or whether the same sample was measured repeatedly
- The statistical test(s) used AND whether they are one- or two-sided
Only common tests should be described solely by name; describe more complex techniques in the Methods section.
- A description of all covariates tested
- A description of any assumptions or corrections, such as tests of normality and adjustment for multiple comparisons
- A full description of the statistical parameters including central tendency (e.g. means) or other basic estimates (e.g. regression coefficient) AND variation (e.g. standard deviation) or associated estimates of uncertainty (e.g. confidence intervals)
- For null hypothesis testing, the test statistic (e.g. F , t , r) with confidence intervals, effect sizes, degrees of freedom and P value noted
Give P values as exact values whenever suitable.
- For Bayesian analysis, information on the choice of priors and Markov chain Monte Carlo settings
- For hierarchical and complex designs, identification of the appropriate level for tests and full reporting of outcomes
- Estimates of effect sizes (e.g. Cohen's d , Pearson's r), indicating how they were calculated

Our web collection on [statistics for biologists](#) contains articles on many of the points above.

Software and code

Policy information about [availability of computer code](#)

Data collection

Data was collected from a customized PC scripts developed using Python 2 (Python Org).

Data analysis

Data analysis was performed using Python 2 and 3 (Python Org) and MATLAB (MathWork).

For manuscripts utilizing custom algorithms or software that are central to the research but not yet described in published literature, software must be made available to editors/reviewers. We strongly encourage code deposition in a community repository (e.g. GitHub). See the Nature Research [guidelines for submitting code & software](#) for further information.

Data

Policy information about [availability of data](#)

All manuscripts must include a [data availability statement](#). This statement should provide the following information, where applicable:

- Accession codes, unique identifiers, or web links for publicly available datasets
- A list of figures that have associated raw data
- A description of any restrictions on data availability

The authors declare that data supporting the findings of this study are available within the paper and its supplementary information files.

Field-specific reporting

Please select the one below that is the best fit for your research. If you are not sure, read the appropriate sections before making your selection.

- Life sciences Behavioural & social sciences Ecological, evolutionary & environmental sciences

For a reference copy of the document with all sections, see nature.com/documents/nr-reporting-summary-flat.pdf

Life sciences study design

All studies must disclose on these points even when the disclosure is negative.

Sample size	Sample size of total of 50 subjects have been used in this study. Each subset group with different sample size was used to derive different conclusion and the details about number of sample size is described in all relevant places.
Data exclusions	No data was excluded.
Replication	Authors confirm that data used for making conclusions in this manuscript can all be replicated.
Randomization	This is not relevant to this study. We conducted a prospective, observational single-arm study to evaluate the safety and performance of our sensors. Thus, randomization was not necessary or appropriate.
Blinding	We conducted a prospective, observational single-arm study to evaluate the safety and performance of our sensors. Nurses / patients / clinicians were not blinded to use of the sensors.

Reporting for specific materials, systems and methods

We require information from authors about some types of materials, experimental systems and methods used in many studies. Here, indicate whether each material, system or method listed is relevant to your study. If you are not sure if a list item applies to your research, read the appropriate section before selecting a response.

Materials & experimental systems

n/a	Involved in the study
<input checked="" type="checkbox"/>	<input type="checkbox"/> Antibodies
<input checked="" type="checkbox"/>	<input type="checkbox"/> Eukaryotic cell lines
<input checked="" type="checkbox"/>	<input type="checkbox"/> Palaeontology
<input checked="" type="checkbox"/>	<input type="checkbox"/> Animals and other organisms
<input type="checkbox"/>	<input checked="" type="checkbox"/> Human research participants
<input type="checkbox"/>	<input checked="" type="checkbox"/> Clinical data

Methods

n/a	Involved in the study
<input checked="" type="checkbox"/>	<input type="checkbox"/> ChIP-seq
<input checked="" type="checkbox"/>	<input type="checkbox"/> Flow cytometry
<input checked="" type="checkbox"/>	<input type="checkbox"/> MRI-based neuroimaging

Human research participants

Policy information about [studies involving human research participants](#)

Population characteristics	Any patient admitted to the neonatal or pediatric intensive care units were eligible for participation. The only exclusions were active hemodynamic instability or active skin infection.
Recruitment	Patients were recruited following strict guidelines by the Northwestern Institutional Review Board. Subjects were first screened by a trained research assistant. Their appropriateness was then confirmed by the primary clinical team. After, patients and their parents were approached for consent.
Ethics oversight	Northwestern University and Ann & Robert H. Lurie Children's Hospital (STU00202449)

Note that full information on the approval of the study protocol must also be provided in the manuscript.

Clinical data

Policy information about [clinical studies](#)

All manuscripts should comply with the ICMJE [guidelines for publication of clinical research](#) and a completed [CONSORT checklist](#) must be included with all submissions.

Clinical trial registration	NCT02865070
Study protocol	The study protocol is available online at clinicaltrials.gov NCT02865070
Data collection	Subjects were recruited with data collected within 7 calendar days. All recruitment occurred either at the Ann & Robert H. Lurie Children's Hospital neonatal ICU or pediatric ICU.
Outcomes	Primary outcomes: heart rate, respiratory rate, temperature and pulse oximetry agreement with gold standard monitoring systems. Secondary outcomes: parental preference, nursing preference, skin safety post sensor removal, non-invasive blood pressure correlation with arterial line data, crying time correlation with manual determination, and body position categorization accuracy